SCIENCE CHINA
Earth Sciences

•ARTICLE•

August 2025 Vol.68 No.8: 2591–2614
https://doi.org/10.1007/s11430-024-1609-2

Characterizing the migration of deep materials beneath the Xainza-Dinggye rift and the seismogenic environment in the southern Tibetan Plateau: Insights from a 3-D electrical resistivity model

Yue SHENG[1,3], Sheng JIN[1,2,3*], Zengqian HOU[4*], Matthew J. COMEAU[5], Michael BECKEN[6], Wenbo WEI[1,3], Gaofeng YE[1,3], Letian ZHANG[1,3], Hao DONG[1,3], Yaotian YIN[1,3], Chengliang XIE[1,3] & Jian'en JING[1,3]

[1] *School of Geophysics and Information Technology, China University of Geosciences, Beijing 100083, China*
[2] *School of Geoscience, Hebei GEO University, Shijiazhuang 050031, China*
[3] *Key Laboratory of Intraplate Volcanoes and Earthquakes (China University of Geosciences, Beijing), Ministry of Education, Beijing 100083, China*
[4] *Institute of Geology, Chinese Academy of Geological Sciences, Beijing 100037, China*
[5] *Department of Geoscience and Engineering, Delft University of Technology, Delft 2628 CN, The Netherlands*
[6] *Institut für Geophysik, Universität Münster, Münster 48159, Germany*

Received December 3, 2024; revised April 30, 2025; accepted June 4, 2025; published online July 21, 2025

Abstract Since the Cenozoic, a series of extensional south-north normal faults and gneiss-granite domes evolved in the southern Tibetan Plateau, the formation mechanism of which is of scientific interest and which has implications for the tectonic dynamics of the plateau. Typical of such features are the Xainza-Dinggye rift and the Mabja gneiss dome, which are located in the Xainza-Xietongmen-Dinggye region in the central Tibetan Plateau. In this study, Magnetotelluric measurements across this region are used to generate a high-resolution 3-D electrical resistivity model of the subsurface and to analyze the cause of the conductive zones. The large-scale conductive zones identified in the middle-lower crust may result from aqueous melt partial melting, whereas the smaller-scale conductive zones in the upper-middle crust may result from saline fluids, possibly with varying minor volumes of melts. Subsequently, based on the electrical resistivity model and combined with the spatiotemporal coupling of the geological, geochemical, and geophysical data, the state and migration features of crustal materials are discussed. The results show that the upwelling of mantle materials along subduction channels and slab-windows related to the tearing of the Indian lithospheric plate contributed to the partial melting of the middle-lower crust in the Lhasa terrane. Furthermore, partial melting of the upper-middle crust in the Tethys-Himalaya terrane resulted from southern extrusion of crustal materials in the Lhasa terrane. These two mechanisms can significantly reduce the effective viscosity. We speculate that the deformation of the brittle upper crust that is controlled by large-scale ductile layers characterized by weak rheology is the main dynamic mechanism of rift evolution. Meanwhile, the metamorphism and anatexis in the upper-middle crust of the Tethys-Himalaya terrane related to the southern extrusion of materials contributed to the evolution of the Mabja gneiss dome. During the middle Miocene, the southern extrusion of crustal materials may have been influenced by the cooling events beneath the Mabja gneiss dome, which can explain why the deep areas beneath the Mabja gneiss dome have middle-high resistivity. In addition, our study region is located in the Mediterranean-Himalayan seismic belt, and mainly includes shallow-focus earthquakes and intermediate-depth earthquakes. In the north, shallow-focus earthquakes are mainly controlled by the accumulation of stress in the brittle layer of the overlying crust related to the ductile layer of the middle and lower crust. In the south, shallow-focus earthquakes (e.g., Dingri M_S6.8 earthquake) mainly occur in the rigid, resistive block, which is surrounded by conductive zones, possibly because fluid

* Corresponding authors: Sheng JIN (1993010830@cugb.edu.cn), Zengqian HOU (houzengqian@126.com)

migration may be hindered by these resistive blocks. The intermediate-depth earthquakes are mainly controlled by the response in the subsurface area, which is related to the detachment of the Indian lithospheric mantle from the Indian crust.

Keywords Tibetan Plateau, Magnetotellurics, Xainza-Dinggye rift, Mabja gneiss dome, Material migration, Seismogenic environment, Dingri earthquake

Citation: Sheng Y, Jin S, Hou Z, Comeau M J, Becken M, Wei W, Ye G, Zhang L, Dong H, Yin Y, Xie C, Jing J. 2025. Characterizing the migration of deep materials beneath the Xainza-Dinggye rift and the seismogenic environment in the southern Tibetan Plateau: Insights from a 3-D electrical resistivity model. Science China Earth Sciences, 68(8): 2591–2614, https://doi.org/10.1007/s11430-024-1609-2

1. Introduction

The Tibetan Plateau is a natural field laboratory for studying the relationships of various geological processes that occurred in the collision orogeny (Yin and Harrison, 2000; Tapponnier et al., 2001; Yin, 2004; Xu et al., 2006, 2016; Zhu et al., 2012, 2013). From south to north, the Tibetan Plateau consists of the Himalaya terrane, Lhasa terrane, Qiangtang terrane, and Songpan-Ganzi terrane, and those terranes are separated by the Indus-Yarlung Zangbo suture, Banggong Tso-Nujiang River suture, and Jinsha River suture (e.g., Chang, 1985; Zhu et al., 2011, 2012). Since the Mesozoic, the southern part of the Tibetan Plateau (including the Lhasa terrane and Himalaya terrane) has experienced a series of tectonic events related to the subduction of the Bangong Tso-Nujiang Tethyan Ocean, collision of the Lhasa-Qiangtang terranes, subduction of the Neo-Tethyan Ocean, and collision of the Indian-Eurasian plates. The tectonic processes in the subsurface controlled by these events have been of significant scientific interest and widely debated.

A series of extensional south-north normal faults (rifts) and gneiss-granite domes in the south Tibetan Plateau are some of the most extensive and distinctive structures developed on the Tibetan Plateau (Hou et al., 2001; Zhang, 2007). Among them, the south-north rifts evolved in the Lhasa and Tethys-Himalaya terranes, including Yari rift, Longger rift, Nima-Dingri rift (Dangreyongcuo rift), Xainza-Dinggye rift (XDR), Yadong-Gulu rift, and Riduo-Cuona-Woka rift (Chen et al., 2015), and the formation ages of these rifts gradually become younger from west to east (Chung et al., 2005; Hou et al., 2015; Bian et al., 2020). Furthermore, dome structures that have a beaded, discrete distribution have developed in the Tethys-Himalaya terrane, and the Northern Himalayan gneiss dome belt (NHGD). The Himalayan leucogranite belt, which is composed of dome structures and exposed leucogranite within (Yin, 2004; Wu et al., 2015), is crucial to understanding the metamorphic-deformation and anatexis in the Himalayan orogenic process, and is an important district to study processes including continent-continent collision, orogenic cycle, crust-mantle rheology, and deep thermal-dynamic process (Chen et al., 2022). Previous studies reported that older domes (e.g., the Yalaxiangbo, Kangmar, Mabja, Kampa, and Malashan domes) developed by a dominantly north-south-oriented shortening and local extension regime, while younger domes (e.g., the Ranba, Leo Pargil, and Gurla Mandhata domes) appear to have predicted a neotectonic phase of east-west extension, and are always accompanied with a roughly north-south-trending regional graben and north-south-trending normal faults (Fu et al., 2017).

Work by others has generated various models to explain the formation of the south-north faults (rifts), including models such as radial extension fracture (Kapp and Guynn, 2004), block extrusion (Armijo et al., 1986), gravity collapse (Molnar and Tapponnier, 1978), lateral material flow (Tapponnier et al., 1982; Lee and Whitehouse, 2007), mantle convection (Yin and Harrison, 2000), and plate tearing (Chen et al., 2015; Bian et al., 2020). Despite this, the formation mechanism of these south-north normal faults (rifts) is still controversial. Furthermore, several mechanisms have also been proposed to explain the origin and evolution of the gneiss domes, including the thrust structure or duplexing structure (Burg et al., 1984), crust anatexis and magma underplating (Ramberg, 1980; Calvert, 2017; Teyssier and Whitney, 2002; Whitney et al., 2004), and middle crustal flow (Nelson et al., 1996; Beaumont et al., 2001; Grujic et al., 2002; Langille et al., 2010). In addition, more research now points to explaining the evolution of the gneiss domes with a combination of multiple models, instead of a single model (Lee et al., 2000, 2006; Zhang, 2007; Zhang et al., 2012). Hence, although a series of tectonic-dynamic models explaining the south-north normal faults and gneiss domes have been put forward, it is still necessary to discuss the spatiotemporal relationship of the south-north normal faults and gneiss domes, and their relationship with the state and migration of crustal materials.

In this paper, the Xainza-Xietongmen-Dinggye region, including the Xainza-Dinggye rift and Mabja gneiss dome, is chosen as the study area. Although much work related to geological, geochemical, geophysical, and numerical modelling has been carried out, the formation mechanism of the northern segment (mainly located in the Lhasa terrane) and the southern segment (mainly located in the Tethys-Himalaya terrane) of the Xainza-Dinggye rift has not been comprehensively reviewed. On the other hand, because of the scarcity of deep geophysical research, there is a lack of in-

formation about the deep structural and rheological features beneath the gneiss dome. This has restricted studies on the relationship between the lithospheric material state and migration and the deep mechanism of the Xainza-Dinggye rift and Mabja gneiss dome. Meanwhile, the Xainza-Xietongmen-Dinggye region in the southern area of the Himalya orogenic belt is also the region where earthquakes occur frequently, and the moderate-strong earthquakes have been active in this region (Liang et al., 2008; Wang et al., 2015; Klemperer et al., 2022). Therefore, the seismogenic environment in the Xainza-Xietongmen-Dinggye region must also be paid more attention.

Previous studies have reported that deep-seated dynamic processes contributed to the large-scale extensional structures, and the lithospheric structure beneath and in the vicinity of rifts was a key factor in studying the formation of rifts and tectonic dynamic processes (Hou et al., 2020). The magnetotelluric method (MT) can probe the subsurface electrical resistivity structure throughout the lithosphere (Chave and Jones, 2012). This property is sensitive to temperature and rheology (Wei et al., 2001; Unsworth et al., 2005). Therefore, an array of MT measurements covering the Xainza-Xietongmen-Dinggye region is used to establish a high-resolution electrical resistivity model of the lithosphere. In combination with identifying the subsurface distribution of resistivity and rheology in this region, the present study aims to provide new insights on deep-seated dynamic mechanisms related to surface deformation, extensional structure formation, and seismogenic environment.

2. Geological background

The Xainza-Xietongmen-Dinggye region is located in the central-southern Tibetan Plateau. The study area lies within the following geographical coordinates: latitude 27.5°N–31°N and longitude 87°E–89°E (Figure 1b; red rectangle). This region includes parts of the central Lhasa terrane, the southern Lhasa terrane, the Tethys-Himalaya terrane, and the High Himalaya terrane. Magmatic rocks of neutral-acid composition have formed in the Yanshanian (with tectonic dynamics during the Jurassic-Cretaceous) and Xishan (tectonic dynamics during the Cenozoic) period and are widely distributed in this region, with the typical magmatic rocks being the Gangdese Lizizong granite and North-Himalayan leucogranite (Zhu et al., 2011; Hou et al., 2015). The Xainza-Dinggye rift, which is typical of the various north-south-directed rifts in the southern part of Tibetan Plateau, has evolved in an extension background related to the movement of the Indian-Eurasian plates during the Miocene, and the formation age was ~13–10 Ma (Zhang, 2002; Zhang and Guo, 2007). The XDR is located south of Xainza city, its northern boundary intersects with the Gyaring Co fault (a V-shaped conjugate strike-slip fault) in the Lhasa terrane, it crosses southwards the Luobadui-Milashan fault and Indus-Yarlung Zangbo suture, it extends to the Tethys-Himalaya terrane, and it intersects with the south Tibetan detachment system (STDs), which is separated into two parts by the XDR (Figure 1; Zhang and Guo, 2007; Xue et al., 2021). In the Lhasa terrane, the XDR is a brittle fault system with some narrow semi-grabens, and the main fault is mainly in its western boundary (Zhang and Guo, 2007). In the Tethys-Himalaya terrane, the southern part of the XDR consists of an early dome structure and a later normal fault that was covered by Paleozoic syenite and metasedimentary rocks. The dome structure is the Mabja gneiss dome, which is a typical one of the NHGD. The Mabja gneiss dome is located east of the XDR, and is characterized by a core of Tertiary migmatitic orthogneiss mantled by Paleozoic orthogneiss and metasedimentary rocks that in turn are overlain by Triassic and Jurassic metasedimentary and sedimentary rocks (Langille et al., 2010). In the High Himalaya terrane, the XDR consists of southeast-trending normal faults similar to the detachment fault (Zhang and Guo, 2007).

Tectonic movement in the Xainza-Xietongmen-Dinggye region is still ongoing, and several earthquakes of magnitude 7.0 or greater have occurred since the 20th century; in fact, it is one of the most active areas of moderate-to-strong earthquakes in the Tibetan Plateau. The hypocenters of the intermediate-depth earthquakes are 65–100 km below the surface (Klemperer et al., 2022), and the hypocenters of the shallow-focus earthquakes are 20–30 km below surface (Liang et al., 2008). Furthermore, some earthquakes of magnitude 4–5 with the hypocenter depths of 6–10 km have also occurred in this region. The earthquakes related to the Xainza-Dinggye normal faults belong to the category of shallow-focus earthquakes (Chang et al., 2017), and frequent small earthquakes show that this normal fault is one of the most active structures in the southern Tibetan Plateau. In addition, the activity of surface water is pronounced in this region, in which hot springs have various significant features (Hou et al., 2001; Hou and Li, 2004; He et al., 2017). The features of geothermal activity can be summarized as (1) widespread distribution and variety; (2) close relationship between the hydrothermal activities and the tectonic activities; (3) consistent distribution of geothermal and seismic areas, and close association of the hot springs and earthquakes (Zou et al., 2023).

3. Data and inversion

3.1 Data analysis

In this study, 126 MT measurements with an average spacing of 5–10 km covering the Tethys-Himalaya terrane, southern Lhasa terrane, and northern Lhasa terrane are used. The MT

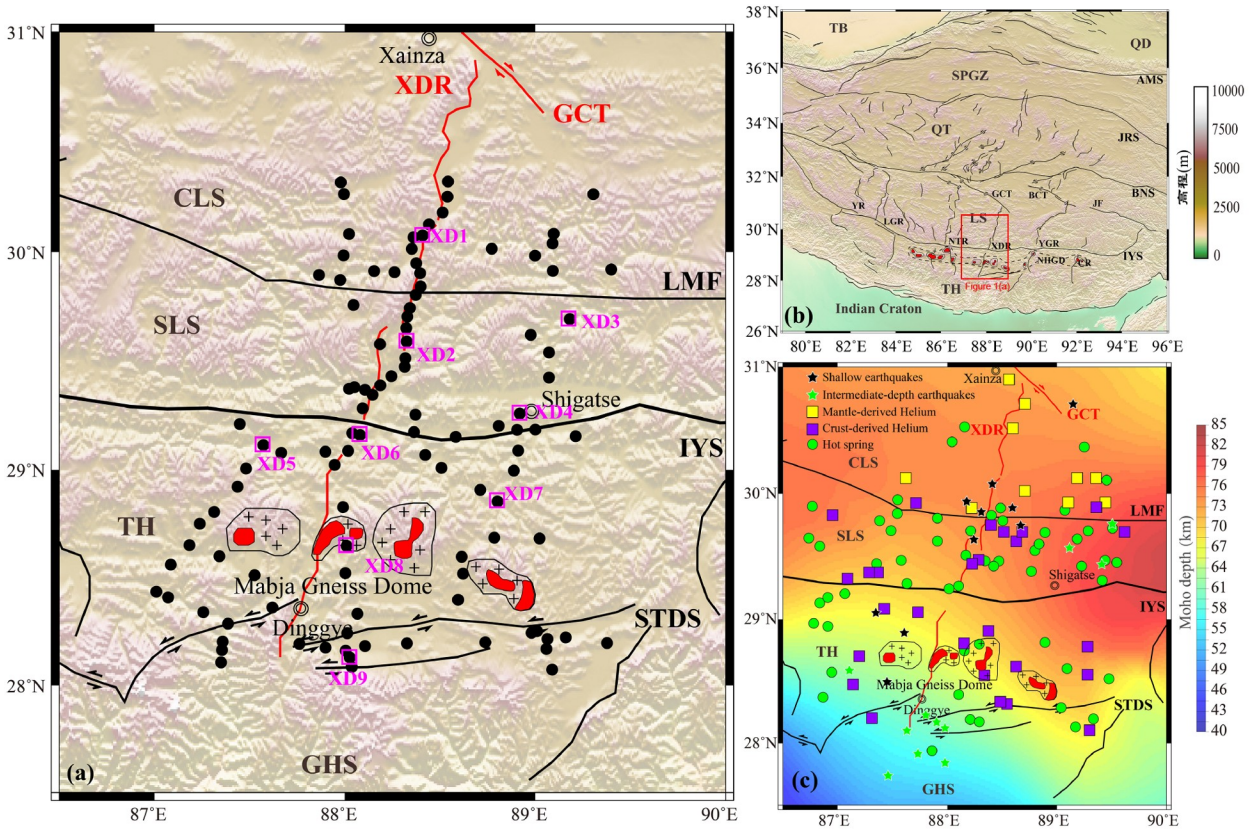

Figure 1 Distribution of the MT measurements in the study area. (a) The locations of the MT measurements are marked with black dots. The pink label XD1–XD9 refers to typical MT stations shown in Figure 2. The Xainza-Dinggye rift and Mabja gneiss dome are derived from Yin and Harrison (2000), Zeng et al. (2011), and Bian et al. (2020). (b) Topography of the Tibetan Plateau and its adjacent areas. The red rectangle outlines the study area. (c) Distribution of the Moho depth in the study area (modified from Li et al., 2014). Locations of the intermediate-depth earthquakes (green stars), mantle-derived Helium and crust-derived Helium (squares) are derived from Klemperer et al. (2022), and locations of the shallow-focus earthquakes (black stars) are derived from Liang et al. (2008), in which the location of the Dingri M_S6.8 earthquake is derived from the China Earthquake Network. Hot springs (green circles) are derived from He et al. (2017). GHS, Greater Himalaya Sequence; TH, Tethys-Himalaya terrane; LS, Lhasa terrane; SLS, Southern Lhasa terrane; CLS, Central Lhasa terrane; QT, Qiangtang terrane; SPGZ, Songpan-Ganzi terrane; QD, Qaidam basin; TB, Tarim basin; STDS, Southern Tibetan Detachment System; IYS, Indus-Yarlung Zangbo suture; LMF, Luobadui-Milashan Fault; BNS, Banggong Tso-Nujiang River suture; JRS, Jinsha River suture; AMS, Animaqing suture; CR, Riduo-Cuona Rift; YGR, Yadong-Gulu Rift; XDR, Xainza-Dinggye Rift; NTR, Niyima-Tingri Rift; LGR, Longgar Rift; YR, Yari Rift; GCT, Gerencuo fault; BCT, Bengcuo fault.

data were collected with Phoenix MTU-5A/P instruments. With an average recording time of more than 20 h, high quality data were obtained in the period range of 320–0.0003 Hz. Five components of the time-varying electromagnetic field (*Ex*, *Ey*, *Hx*, *Hy*, *Hz*; with *x*, *y*, and *z* being the south-north, east-west, and vertical directions) were recorded. After data collection, the impedance tensors of the MT data were obtained in the standard way with a fast Fourier transform, statistically robust algorithm, and remote reference method (Egbert, 1997).

The apparent resistivity and phase of some typical MT stations (locations in Figure 1) show curves with a clear shape and good continuity, which indicates that the MT data are of good quality (Figure 2). Stations of XD2, XD3, and XD4 are located in the southern Lhasa terrane, and the data show similar features of moderate-high resistivity in the shallow area and low resistivity in the deep area. Station XD6 is located in the vicinity of the IYS, and the apparent resistivity data shows a high-resistivity in the deep area. Stations XD5, XD7, XD8, and XD9 are located in the Tethys-Himalaya terrane, and the apparent resistivity curves have the feature of an upward tail, which indicates a possible high-resistivity block in the deep area.

After obtaining the impedance tensor from the MT data in the frequency domain, the dimensionality of the data must be analyzed in order to determine how best to do the inversion modelling (such as assuming a one-dimensional, two-dimensional, or three-dimensional Earth). Because the phase tensor of the MT data is not easily affected by distortion, it has been widely used for dimensional analysis. The results of the phase tensor can be represented by an ellipse, and the polarization direction of the phase tensor is the principal axis direction (Caldwell et al., 2004; Booker, 2014). The ellipse of the phase tensor can also be colored by the skew angle β. When the absolute value of the skew angle $|\beta|$ is equal to 0° and the lengths of the major and minor axes of the ellipse are

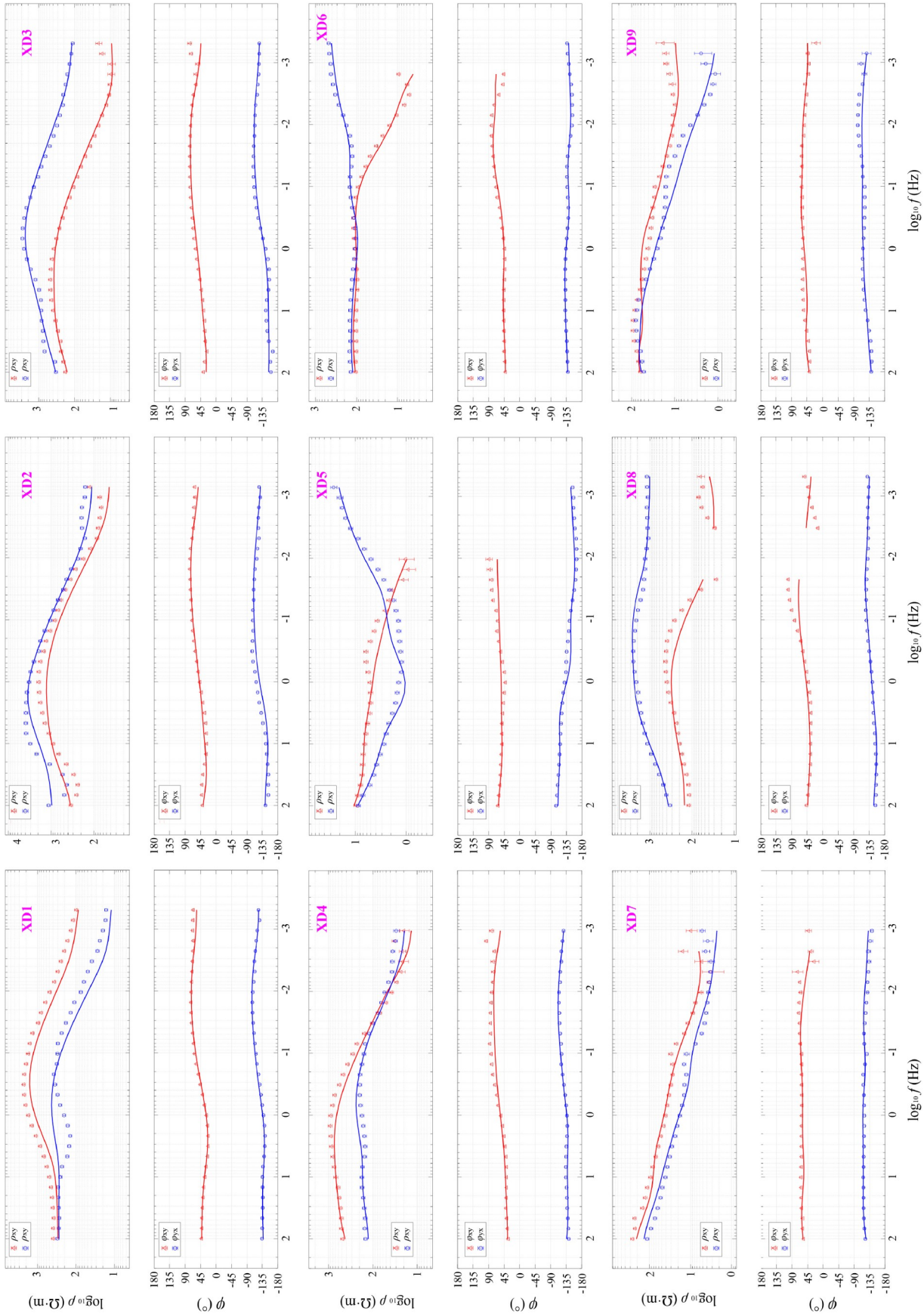

Figure 2 Typical apparent resistivity and impedance phase data (dots). The blue and red colors denote two different modes. The lines are from the 3-D model. A good fit between data and model is observed.

similar (approximately circular), the MT data indicate a one-dimensional assumption is valid; when the absolute skew angle $|\beta|$ is equal to 0° and the lengths of the major and minor axes of the ellipse are unequal, the MT data indicate that a two-dimensional investigation is necessary; when the absolute skew angle $|\beta|$ is not equal to 0°, the MT data indicate that a full three-dimensional treatment is needed (Caldwell et al., 2004; Booker, 2014). Some authors use a threshold and argue that, for example, when the absolute skew angle $|\beta|$ is less than 5°, the MT data can be considered as two-dimensional (Liang et al., 2018). The results of the MT data indicate that in the high-frequency band, the absolute skew angles $|\beta|$ are less than 5° in the whole; in the medium and low-frequency bands, the absolute skew angles $|\beta|$ of most MT data are more than 5°. Combined with the distribution of the MT stations in an array, full 3-D modelling of the MT data is ideal and thus is carried out.

The induction vector is calculated with the vertical component of the magnetic field, which is sensitive to the horizontal variation of resistivity and reverses direction above an electrical interface, boundary, or gradient. Under the Parkinson convention, the arrows of the induction vector point to the direction of the current convergence (Parkinson, 1959). In the high-frequency band, the arrows of the induction vector have no consistency of direction, which may result from the limited probing depth of the high-frequency MT data, and thus the shallow area of crust has two-dimensional and three-dimensional features. In the medium-frequency band, the arrows of the induction vectors in the Tethys-Himalaya terrane point towards the dome structures, which indicates that the deep area in the upper crust (according to the skin depth; Wei et al., 2010) in the vicinity of the Mabja gneiss domes are conductive, while in the Lhasa terrane, the arrows point to the southern and central Lhasa terrane, which indicates conductive zones in the upper crust of the southern and central Lhasa terrane. When the frequency is 0.01 Hz (Figure 3e), the arrows of the induction vectors in the Lhasa terrane are perpendicular to the strike of the IYS, and point towards the southern Lhasa terrane and the IYS, while those in the Tethys-Himalaya terrane are perpendicular to the strike of the IYS, and point to the Tethys-Himalaya terrane, both of which indicate conductive zones in the medium-deep areas of the crust beneath the Tethys-Himalaya and Lhasa terranes. When the frequency is 0.001 Hz (Figure 3f), the arrows mainly point to the central Lhasa terrane, which indicates conductive zones in the deep areas of the crust in the central Lhasa terrane.

3.2 Data inversion

The ModEM algorithm (Egbert and Kelbert, 2012; Kelbert et al., 2014) is used to carry out the 3-D inversion of the MT data, and furthermore, we employed the CPU-GPU hybrid acceleration algorithm based on the unscattered curl-curl equation (Dong et al., 2024). The starting model was a uniform 100 Ω m half space with the number of cells as follows: 111 cells in the north-south direction, 42 cells in the east-west direction, and 69 cells in the vertical direction (in addition to 12 air layers). In the horizontal direction, the grid had a constant cell size of 3.5 km; in the vertical direction the thickness of the first layer was 30 m and increased by a factor of 1.1 in the core region and 1.5 in the padding region. The 3-D inversion used the impedance tensor data (four complex components) and tipper data (from vertical magnetic fields) in a joint inversion. A total of 34 frequency points were used, 6 periods in each decade, logarithmically spaced between 0.01 s and 3000 s. For each impedance component, the error floors were set to 5% of $\sqrt{(|Zxy \cdot Zyx|)}$. An error of 5% on the impedance tensor is equivalent to approximately 2.86° on the phase components and 10% on the apparent resistivity components. Absolute error floors of 0.05 were used for the tipper elements *Tx* and *Ty*. The normalized root-mean-square (nR.M.S.) misfit of the inversion model was reduced from a starting value of 19.2 to 1.90 after 108 iterations.

A comparison of the observed/measured data and the 3-D model response in different frequency bands (10, 0.1, and 0.001 Hz) illustrates the generally good agreement, although several sites have minor differences in the impedance phase (Figure 4). However, the fit of the apparent resistivity and impedance phase at the longest periods (e.g., 1000 s) is observed to be not as good as the shorter periods. This is likely because of the higher errors associated with the long-period data and reflects the reduced resolution of the model in the deep area. The distribution of the site-by-site nR.M.S. shows that the nR.M.S. of most MT stations is less than 3, and the nR.M.S. of one MT station is more than 4, which is because of the cross-quadrant data. Above all, the 3-D inversion model fits the MT data well. Figures 5–7 are the horizontal slices at different depths and vertical sections along different lines from the electrical resistivity model, respectively.

3.3 Sensitivity test

It is reported that signals from the natural electro-magnetic (EM) field can easily penetrate high-resistivity bodies and are sensitive to conductive anomalies (e.g., Zhang et al., 2015). However, the physics of EM signal diffusion in the Earth means that MT data cannot accurately determine the lower boundary of a conductor (Zhang et al., 2015). In order to constrain the electrical boundary of the conductive zones in the model, some new models are established in basis on the 3-D electrical resistivity model. After calculating the responses of each new model, the nR.M.S. misfit of the new forward model and the response curves of MT sites located near the corresponding conductive zones are discussed to verify whether the MT data have good constraints on the

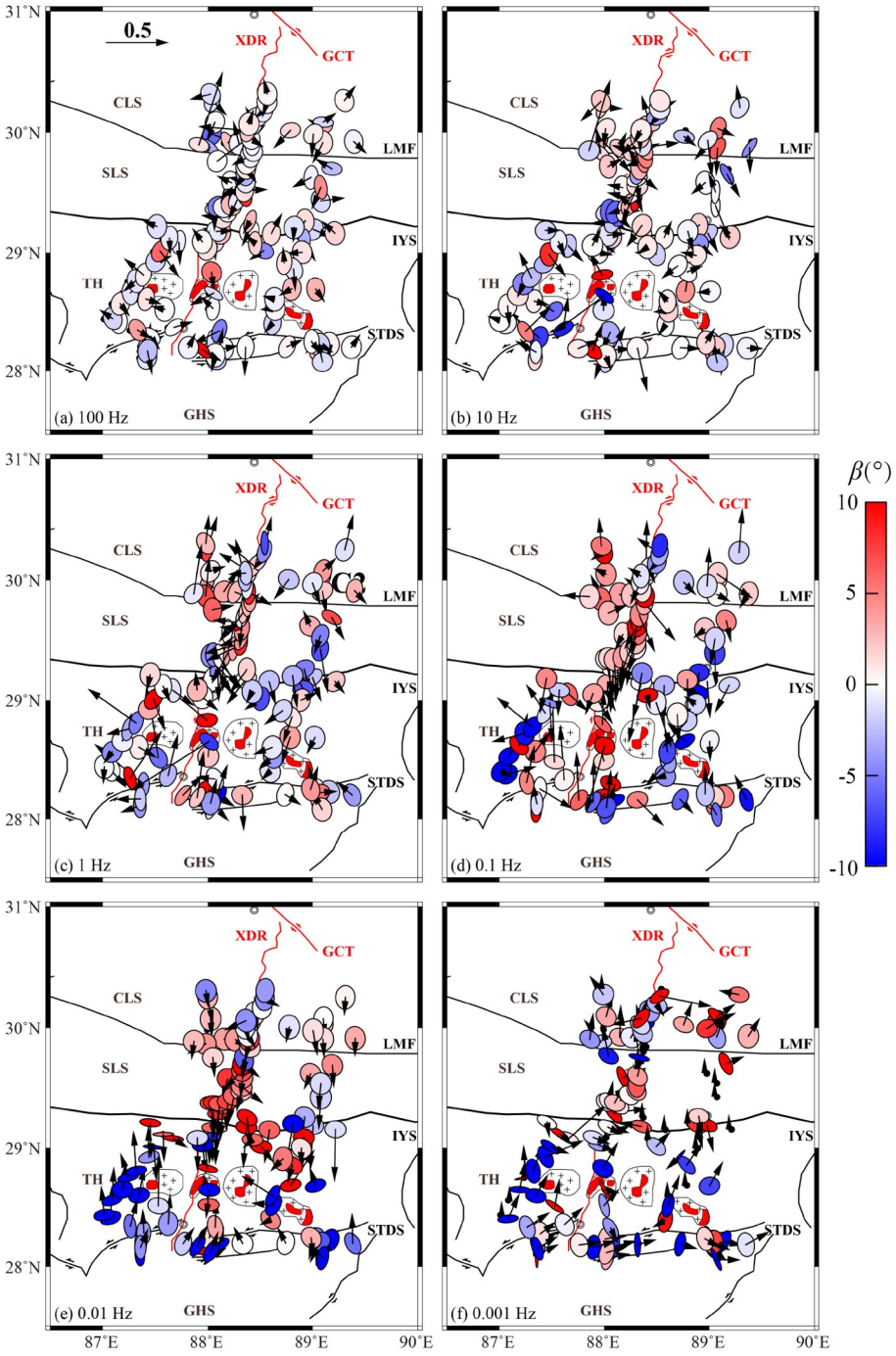

Figure 3 Phase tensor and induction vectors from the MT data.

electrical resistivity model. According to the spatial distribution of the conductive zones, sensitivity tests mainly concentrate on three issues as follows.

(1) Verifying the depth extension of the conductive zones C1 and C2. The conductive zones C1and C2 are replaced with resistive layers (1000 Ω m) at depths of 50 km and 70 km, and new response data are computed through forward modeling. The results show that the nR.M.S. of the MT stations of the new models are significantly different from those of the 3-D model for the conductive zones C1 and C2 (Figure 8). These results indicate that the MT data have good constraints on the bottom boundary of the conductive zones C1 and C2, and the depth extent of these two conductive zones can be 70 km.

(2) Verifying the existence of the medium-high resistivity zones beneath the conductive zone C5 and C7 (whether the conductive zones C5 and C7 are in the upper-middle crust). The resistive zones beneath the conductive zones C5 and C7

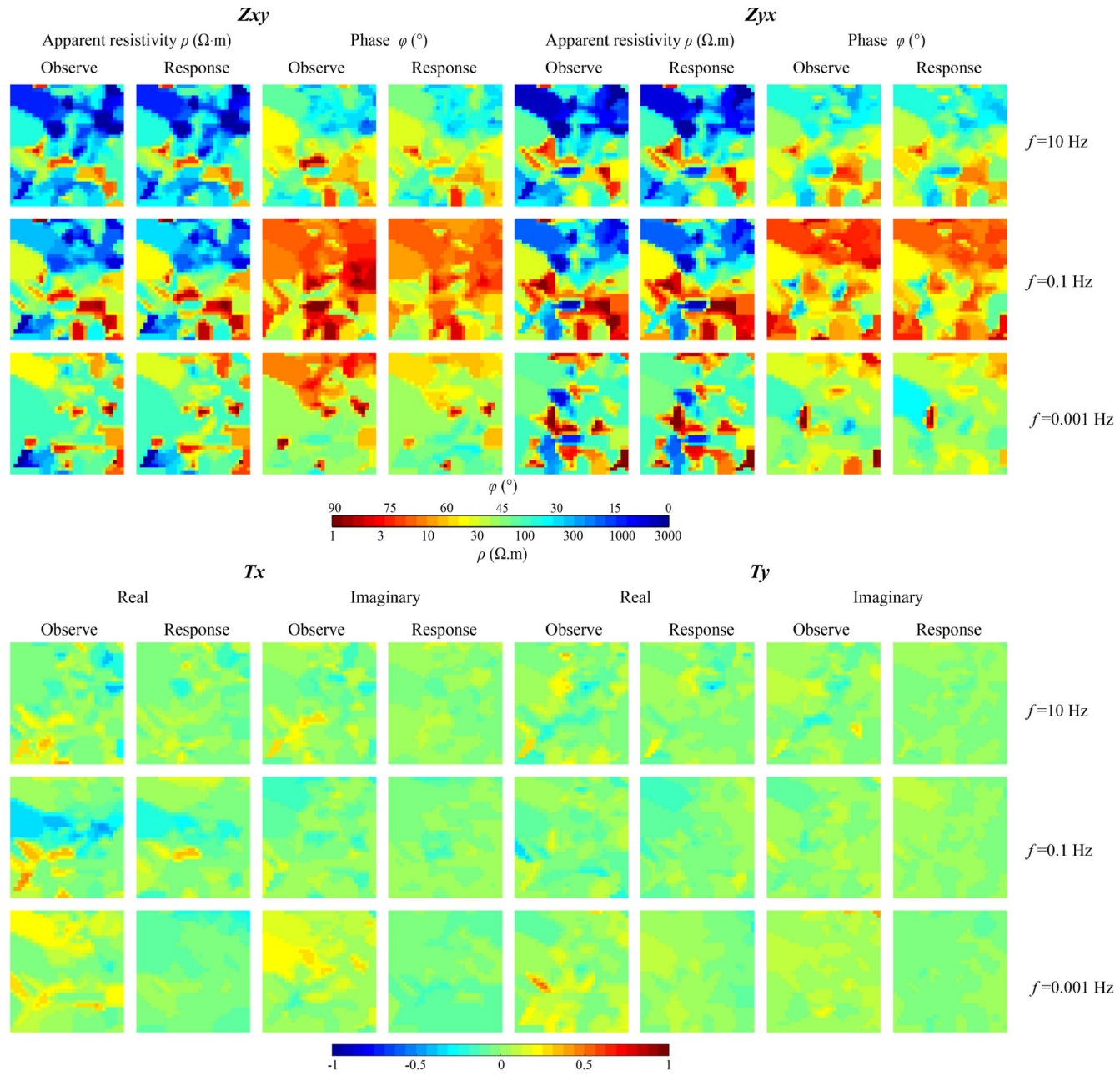

Figure 4 The observed data for impedance and tipper components (for *Zxy*, *Zyx*, *Tx*, and *Ty* components) compared with the 3-D model shown in horizontal pseudo-slice format for different frequencies.

(at depths of more than 30 km) are replaced by zones with a resistivity of 1 Ω m, and new response data are computed through forward modeling. The results show that the nR.M.S. of the MT stations of the new model are significantly different from those of the 3-D model in the conductive zones C5 (Figure 9). These results indicate that the MT data have good constraints on the resistive zones beneath the conductive zones C5, and the conductive zone C5 is mainly located in the upper-middle crust (at depths of less than 30 km). Similarly, the conductive zone C7 is also located in the upper-middle crust.

(3) Verifying the connectivity of the conductive zones C4 and C7 in the upper-middle crust. Two electrical zones with the resistivity of 10 Ω m and 30 Ω m are placed between the conductive zones C4 and C7 at depths of 20–40 km, and new response data are computed through forward modeling. When the resistivity is 10 Ω m in the new model, the nR.M.S. of the MT stations of the new model are significantly different from those of the 3-D model in the vicinity of the conductive zones C4 and C7; When the resistivity is 30 Ω m in the new model, the nR.M.S. of the MT stations of the new model are slightly different from those of the 3-D model in

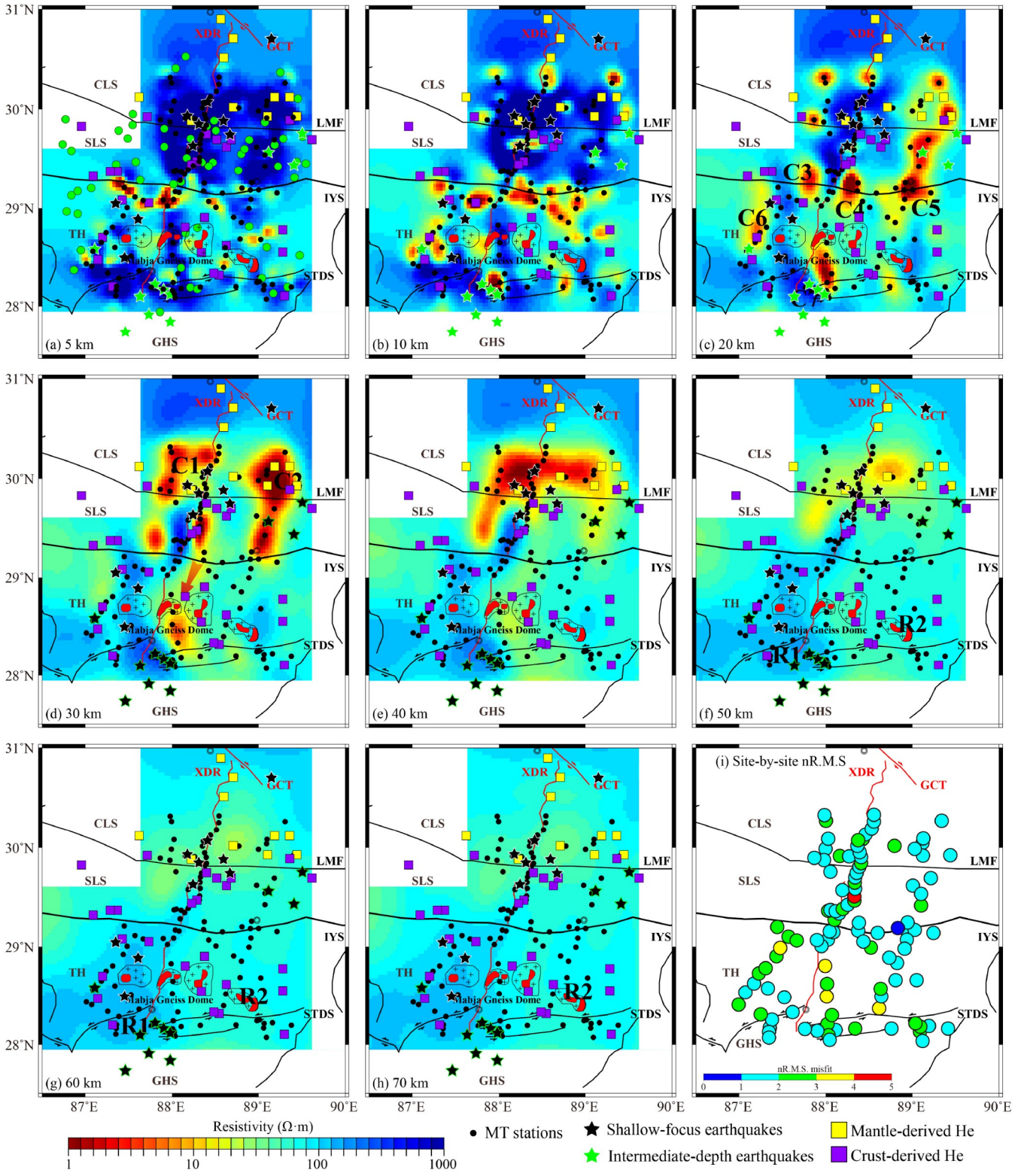

Figure 5 Horizontal slices at different depths of the electrical resistivity model. (a) 5 km; (b) 10 km; (c) 20 km; (d) 30 km; (e) 40 km; (f) 50 km; (g) 60 km; (h) 70 km; (i) site-by-site nR.M.S.

the vicinity of the conductive zones C4 and C7 (Figure 10). These results indicate that the medium-low resistivity zone with a resistivity of 30 Ω m is possibly between the conductive zones C4 and C7 at depths of 20–40 km, that is, the conductive zones C4 and C7 have good connectivity through this zone.

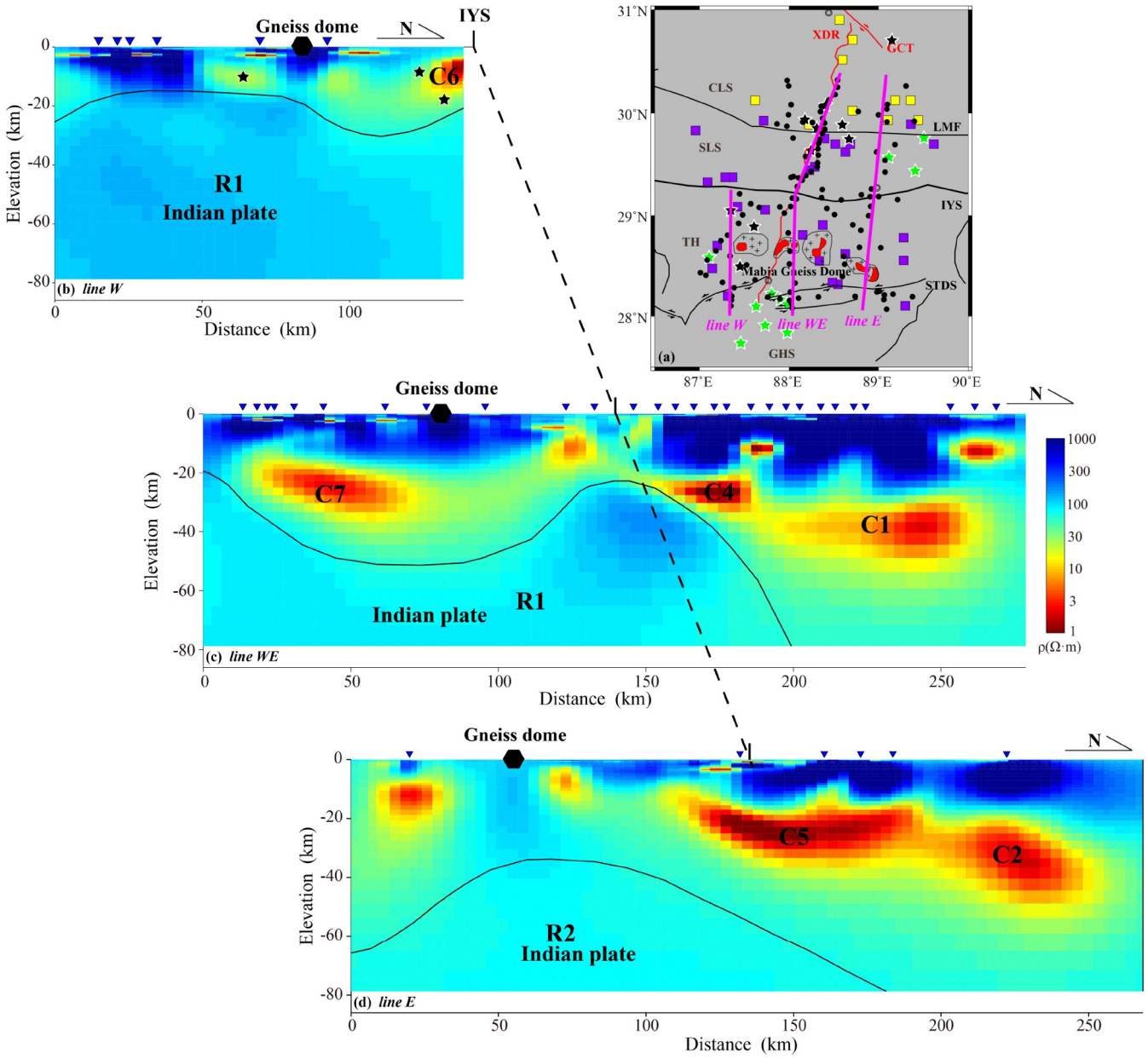

Figure 6 Vertical sections of the electrical resistivity model in the north-south direction. (a) Locations of the vertical sections; (b–d) vertical sections of the electrical resistivity model along different profiles. Black solid lines are the possible top boundary of the large-scale resistive zones in the middle-lower crust.

3.4 Analysis of the electrical resistivity model

Based on the electrical resistivity model, shown as horizontal slices at different depths and vertical sections, two high-resistivity zones (R1, R2) and seven conductive (low-resistivity) zones (C1–C7) are identified.

(1) A large-scale high resistivity zone with a resistivity of more than 1000 Ω m is located at depths of less than 15 km in the upper crust of the Lhasa terrane. Geological data show that Mesozoic-Cenozoic magmatic rocks are widely distributed in the Lhasa terrane, which corresponds well with the resistive zone at depths of less than 15 km. In addition, the uneven bottom of this resistive zone may result from the folding and deformation of the volcanic strata or the growth and deformation of the middle-lower crust.

(2) Both the large-area high resistivity zone and some conductive zones with different scales are distributed at depths of less than 15 km in the upper crust of the Tethys-Himalaya terrane.

(3) The conductive zones C1 and C2 are mainly distributed in the middle-lower crust of the Lhasa terrane, and sensitivity tests show that the depth extent of these conductive zones is 70 km, and meanwhile, these two conductive zones merge into one conductive zone with increasing depth.

(4) The conductive zones C3, C4, and C5 cross the IYS in the north-south direction, and are mainly located at depths of

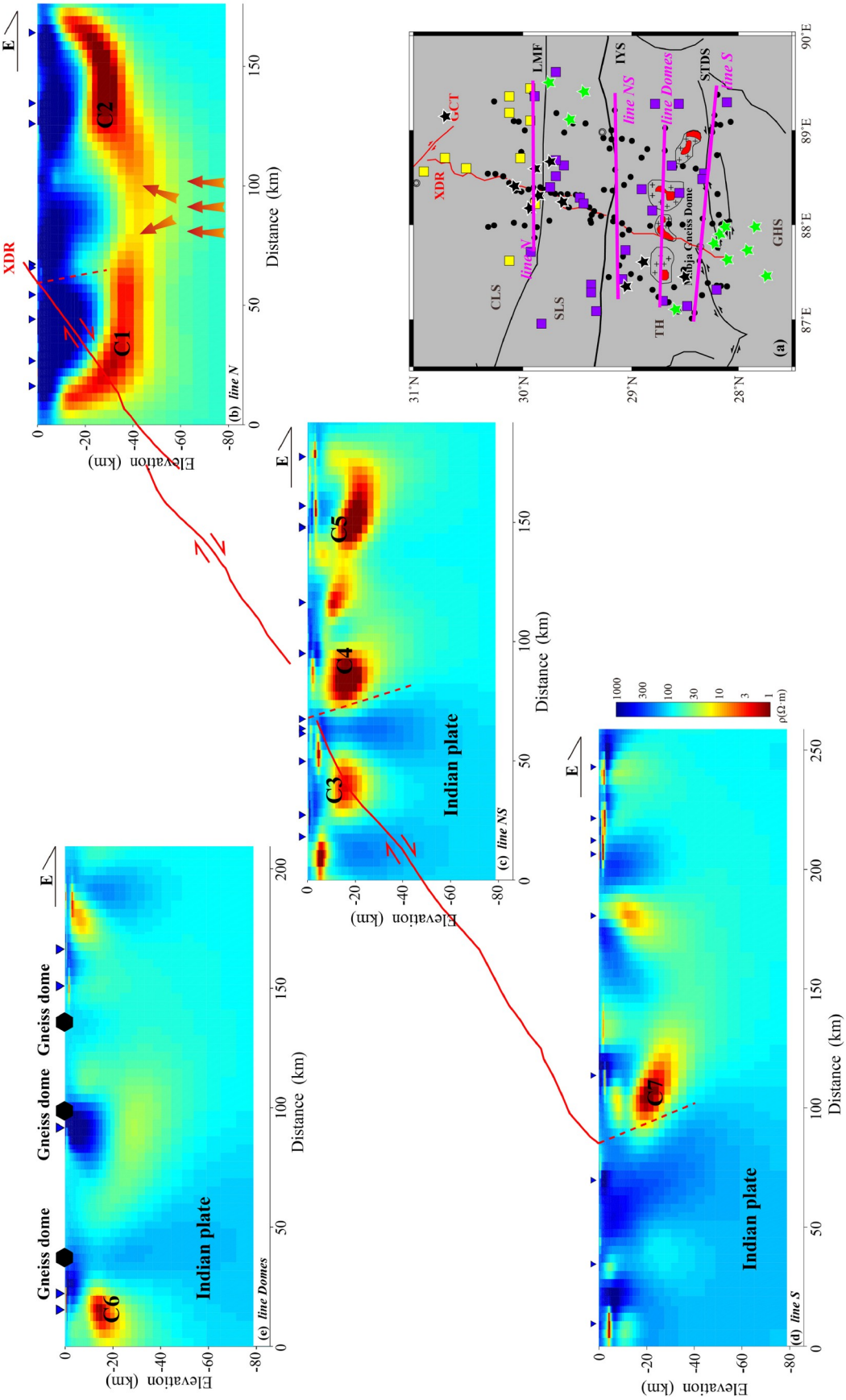

Figure 7 Vertical sections of the electrical resistivity model in the east-west direction. (a) Locations of the vertical sections; (b–e) vertical sections of the electrical resistivity model along different profiles. Red dotted lines are the possible inclination of the Xainza-Dinggye rift. Black solid lines are the possible top boundary of the large-scale resistive zones in the middle-lower crust.

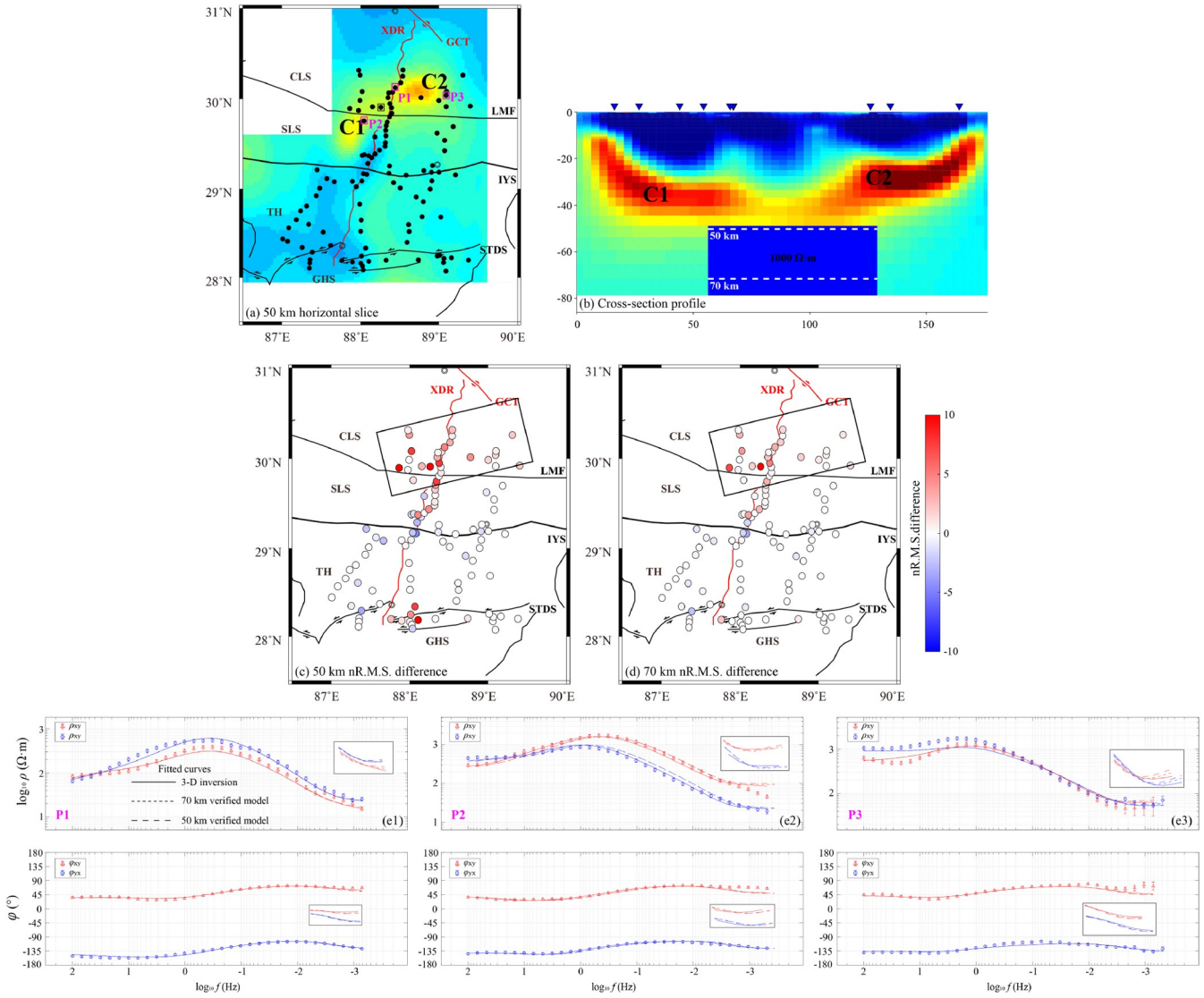

Figure 8 Sensitivity test of the conductive zones C1 and C2. (a) Horizontal slice of the 3-D electrical resistivity model at 50 km depth; (b) verified model; (c, d) are the difference of the nR.M.S of the verified model and 3-D model; (e1–e3) are the comparison of the curves of the apparent resistivity and phase between the verified model and 3-D model. Locations of P1, P2, and P3 are in Figure 8a.

10–40 km. Furthermore, at depth of 30–50 km, these three conductive zones gradually connect with the conductive zones C1 and C2.

(5) The conductive zones C6 and C7 are mainly located at depths of 10–40 km in the upper-middle crust of the Tethys-Himalaya terrane, which also corresponds with some small-scale conductive zones in the shallow area (at depths of less than 5 km).

4. Volume fraction of the melt/fluid based on electrical conductivity

4.1 Conductance and bulk conductivity

In comparison with the electrical resistivity modelled at various depths with the 3-D inversion algorithm, the MT data are generally better at resolving the conductance of a certain layer, in particular conductive ones, instead of the electrical conductivity (conductance is the product of conductivity and thickness; Weidelt, 1985; Jones, 1992). On the other hand, the MT method is a method of volume exploration, and therefore, it is preferred to estimate the volume fractions of melts and fluids (and, by proxy, viscosity) through bulk conductivity derived from conductance (Rippe and Unsworth, 2010; Le Pape et al., 2015).

As conductance is the product of the bulk conductivity of a certain layer and the corresponding layer thickness, the bulk conductivity can be calculated as follows:

$$\sigma_{\text{eff}} = \frac{C}{H}, \tag{1}$$

where C is conductance, and H is the corresponding layer thickness.

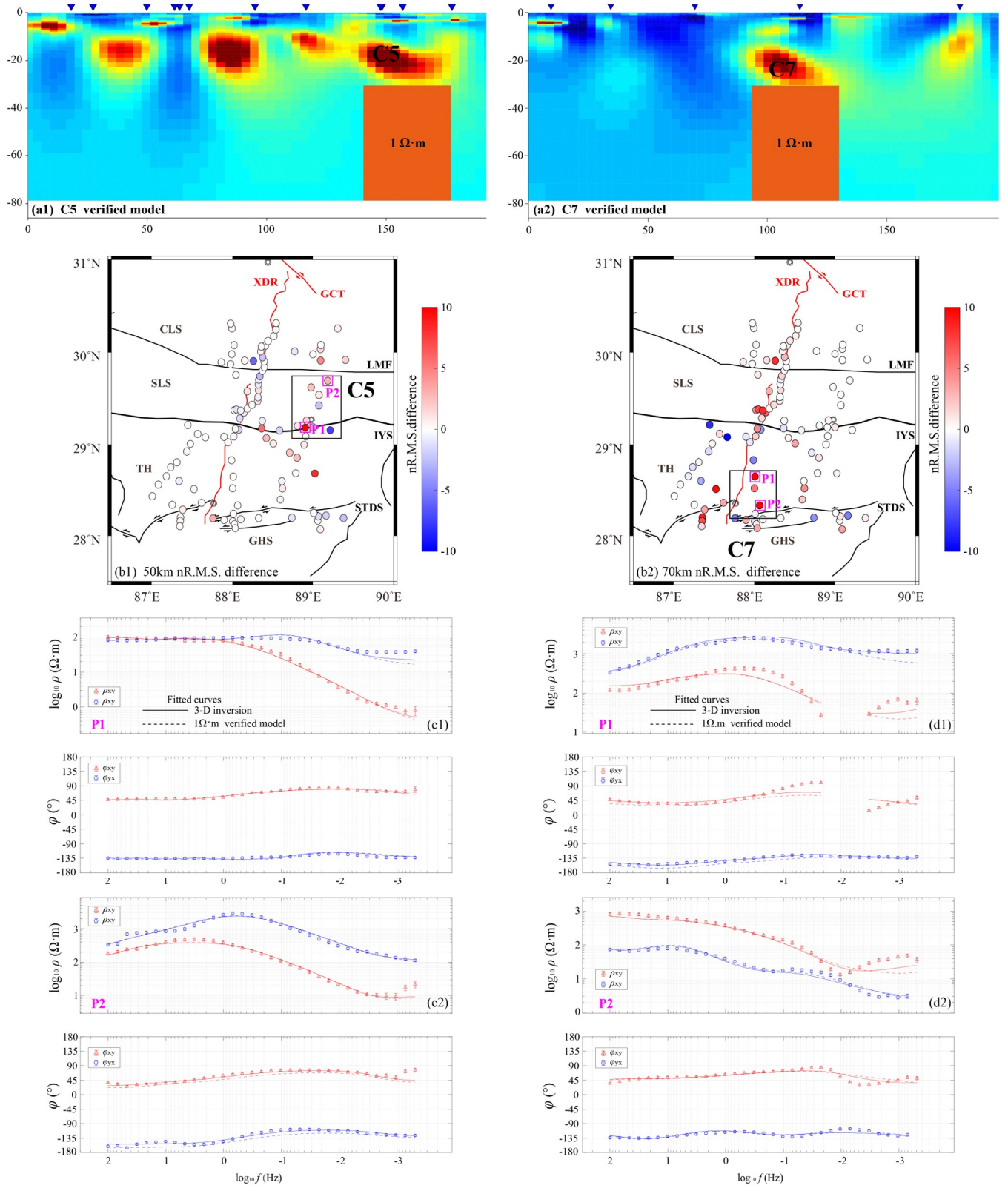

Figure 9 Sensitivity test of the conductive zones C5 and C7. (a1, a2) Verified model; (b1, b2) are the difference of the nR.M.S of the verified model and 3-D model; (c1, c2) are the comparison of the curves of the apparent resistivity and phase between the verified model and 3-D model, for the conductive zone C5. Locations of P1 and P2 are in Figure 9b1. (d1, d2) are the comparisons of the curves of the apparent resistivity and phase between the verified model and 3-D model, for the conductive zone C7. Locations of P1 and P2 are in Figure 9b2.

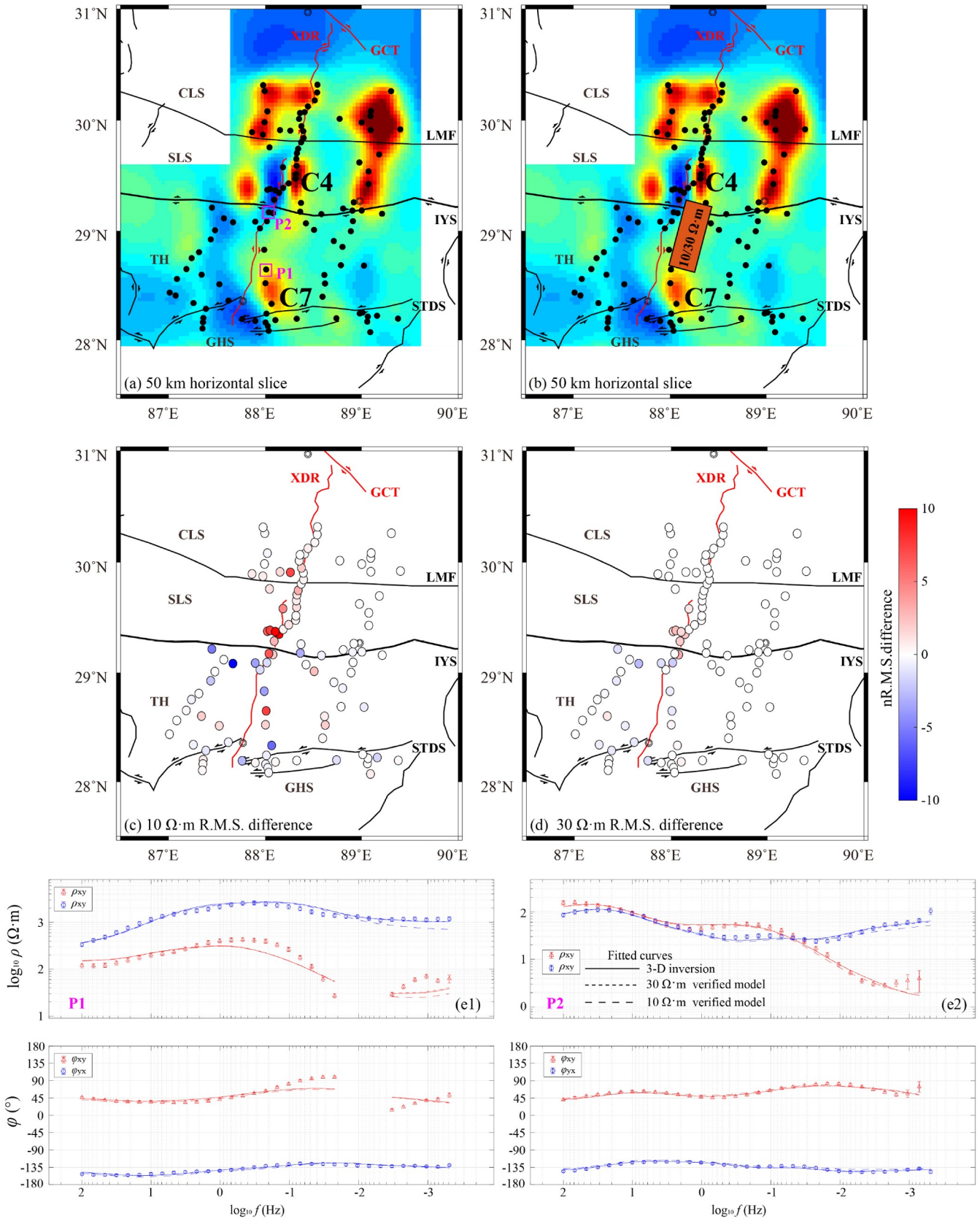

Figure 10 Sensitivity test of the connectivity between the conductive zones C4 and C7. (a) Horizontal slice of the 3-D electrical resistivity model at 50 km depth; (b) verified model; (c, d) are the difference of the nR.M.S of the verified model and 3-D model; (e1, e2) are the comparison of the curves of the apparent resistivity and phase between the verified model and 3-D model. Locations of P1 and P2 are in Figure 10a.

According to the spatial distribution of the conductive zones, the conductance at depths of 10–30 km (upper crust) and 30–70 km (middle-lower crust) are obtained respectively (Figure 11), and the corresponding bulk conductivity is also calculated.

In the middle-lower crust, the maximum conductance value of the conductive zones C1 and C2 is approximately 12,800 S, and the maximum corresponding bulk conductivity is approximately 0.32 S/m (Conductance/layer thickness=12800 S/40000 m). The conductance values of other zones are less than 2000 S. In the upper crust, the conductance values of the conductive zones C5–C7 are at least 9000 S, and the corresponding bulk conductivity is more than 4.5 S/m (conductance/layer thickness=9000 S/20000 m).

The rocks in the crust generally consist of some minerals and aggregates, the bulk conductivity of which is controlled by the combined specific conductivity, volume fraction, mass fraction, and distribution geometry of every mineral and aggregate. If the parameters above are known, the bulk conductivity can be estimated using a mixing model with different phases. Because there are some uncertainties in the calculation of the bulk conductivity of the lithosphere, numerous numerical models have been put forward to estimate the bulk conductivity of materials under different geometric distributions (Archie, 1942; Hashin and Shtrikman, 1962; Somerton, 1992; Luo et al., 1994; Yu et al., 1997; Roberts and Tyburczy, 1999; Glover et al., 2000; Glover, 2010). Among these mixing models, multi-phase Archie's law and the Hashin-Shtrikman upper boundary condition (HS_+) are widely used to discuss the relationship between conductivity and volume fractions of melts/fluids (Sheng et al., 2021, 2023b).

$$\sigma_{HS_+} = \sigma_{melt}\frac{3\sigma_{solid}+2V(\sigma_{melt}-\sigma_{solid})}{3\sigma_{melt}+V(\sigma_{melt}-\sigma_{solid})}, \quad (2)$$

where σ_{HS_+} is the conductivity of the multi-phase system, V is the volume fraction, σ_{melt} is the pure melt conductivity, and σ_{solid} is the conductivity of the rock matrix.

4.2 Formation mechanism of the conductive zones

Previous studies reported that the lithospheric conductive zones below the Tibetan Plateau can mainly be explained by partial melting and water-bearing (saline) fluid (e.g., Wei et al., 2001; Unsworth et al., 2005). As the conductivity of the water-bearing (saline) fluid is higher than that of the silicate melt (in the crust), less volume is required to explain the observations, and it is assumed that the conductive zones resulted from the silicate melt in the beginning. Petrophysical experiments showed that the conductivity of the (water-bearing) silicate melt ranges from 1 to 10 S/m (Li et al., 2003; Unsworth et al., 2005; Wei et al., 2010). Furthermore, Chen et al. (2018) and others reported that with an increasing quantity of dissolved water content in the silicate melt, the conductivity of the melt increases.

According to petrophysical experiments of leucogranite, the conductivity of the rock matrix (background) can be calculated as follows (Hashim et al., 2013; eq. (3)).

$$\sigma_r = 1/\rho_r, \quad \ln\rho_r = -\ln\rho_0 + (-E_a/(RT)), \quad (3)$$

where σ_r and ρ_r are the bulk conductivity and bulk resistivity, ρ_0 is the pre-index constant (Ω m), E_a is the activation energy (J), T is temperature (K), and ln denotes the natural logarithm. According to the results of Hashim et al. (2013), ρ_0 is 2.90±0.20 Ω m and E_a/R can be −8581.80±600.73.

Based on the crustal 2.0 model, Chinese continental geography data, subsurface temperature, and seismic P-wave velocity, the distribution of temperature at different depths in the lithosphere is obtained using the thermal steady-state equation (Sun et al., 2013). This shows that the average temperature at depths of 30–70 km in the middle-lower crust

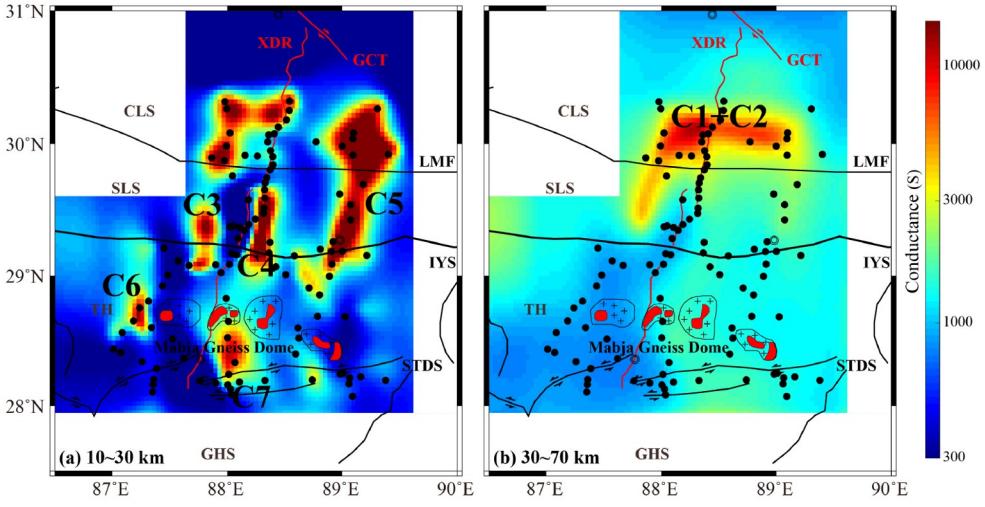

Figure 11 Map of conductance for different depth ranges.

is approximately 950°C, and therefore, the average resistivity of the rock matrix can be 500 Ω m (conductivity of 0.002 S/m). Based on the conductivity at depths of 30–70 km in the middle-lower crust, the volume fractions of melts are estimated using the HS_+ boundary condition (Figure 12). The results show that when the conductivity of pure melt is high (5 S/m or 10 S/m), which occurs when more water content is present in the melts under the same temperature-pressure condition (e.g., Sheng et al., 2021, 2023a), the volume fractions of melts in the conductive zones C1 and C2 can be explained with a value of more than 5%; when the conductivity of pure melt is low (1 S/m), the necessary volume fractions of melts are more than 50%.

The dehydration of some crustal minerals like biotite, Muscovite, or hornblende under low-temperature conditions (approximately 650–750°C) can provide the necessary aqueous fluids for the initial partial melting (Mechie et al., 2004). Furthermore, the aqueous fluids can be released during subduction, e.g., the subsduction of the Indian lithospheric plate, and during this process, the aqueous fluids and aqueous melts (deep thermal materials) can also be miscible, and the miscible materials migrate upwards (e.g., Zheng et al., 2022). Therefore, we can conclude that the conductive zones C1 and C2 probably result from the aqueous melts (partial melting). Additionally, fragmentary materials that resulted from the subduction of the Indian lithospheric plate can also reduce the resistivity of rocks; however, the range of variation would be much smaller than that of melts/fluids

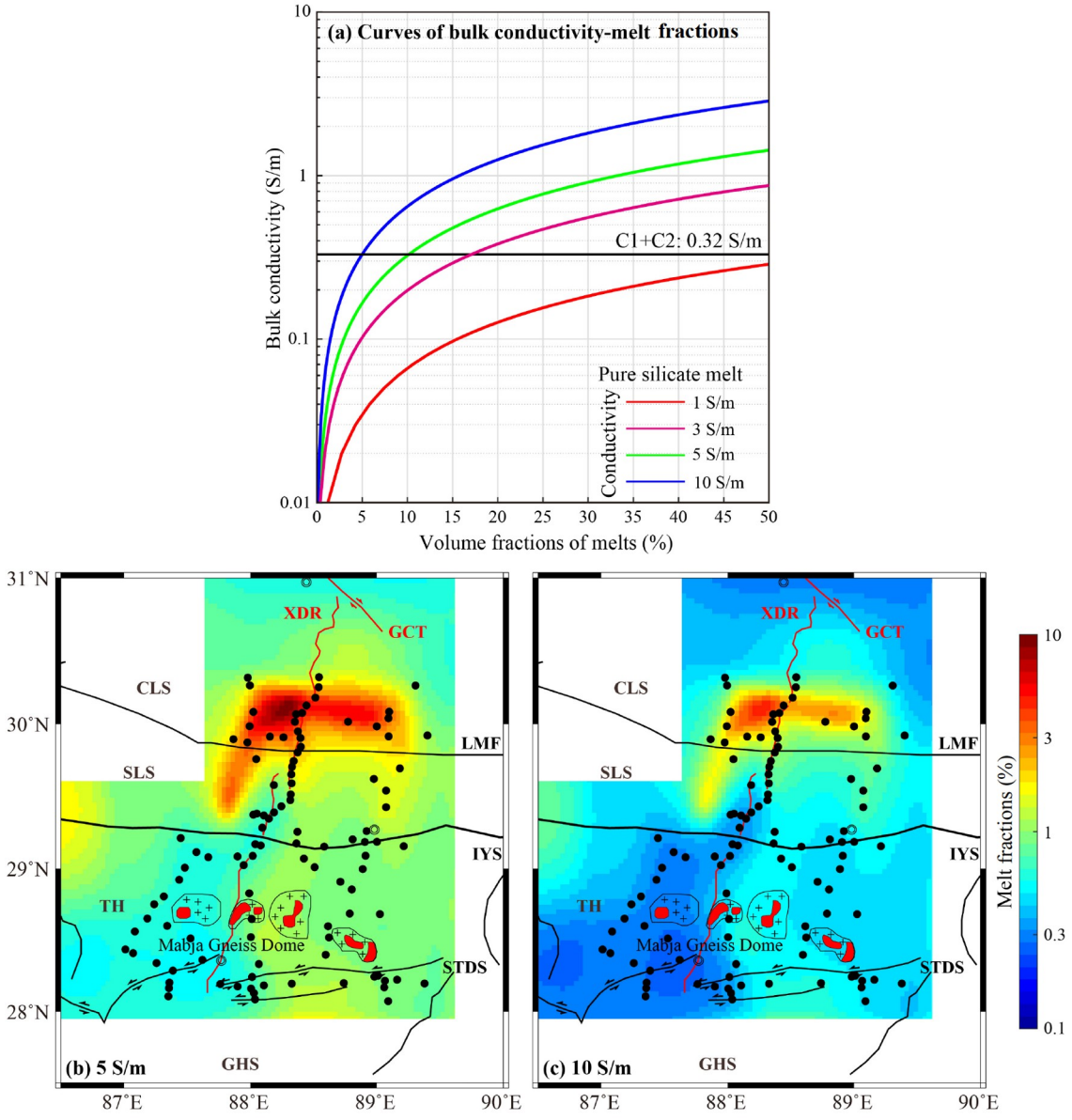

Figure 12 Volume fractions of melts in the middle-lower crust. (a) Curves of bulk conductivity and the volume fractions of melts; (b, c) are the volume fractions of melts in the middle-lower crust when the pure melt conductivity is 5 S/m and 10 S/m, respectively.

(Yang, 2014).

Because the Curie isotherm surface is at depths of 18–23 km (Xiong et al., 2016), the average temperature at depths of 10–30 km can be 600°C, and therefore, the resistivity of the rock matrix at depths of 10–30 km in the upper crust can be approximately 6000 Ω m (conductivity of ~0.0002 S/m). Experimental data showed that when the temperature is 1,200°C, the "dry" rock begins to melt, which increases the conductivity of the rock (Yardley and Valley, 1997). Aqueous fluids play an important role in the melting process. When aqueous fluids are present, the temperature of melting can be significantly reduced (e.g., Unsworth et al., 2005; Ni et al., 2016; e.g., the melting temperature of leucogranite can be reduced to 650°C; Yardley and Valley, 1997). Previous studies indicated that more than 6 wt% water is dissolved in the Himalayan Oligocene-Miocene granite melt (Hashim et al., 2013). Above all, it is assumed that the conductive zones C3–C7 result from aqueous melts, the volume fractions of melts in these conductive zones can be high (Figure 11 based on the high bulk conductivity of these conductive zones (C3–C7; >4 S/m). Chen et al. (2018) reported that if the volume fractions of melts are more than 30% in the crust of the southern Tibetan Plateau, it reflects a crust that is either fluid-enriched or high-temperature. The last magmatic activity in the central Lhasa terrane was mainly during the Paleocene-Eocene (Hou et al., 2015), and when the magmatic activity finished, melts in the upper crust gradually cooled and crystallized, precipitating saline fluids, with a decrease in temperature. Therefore, the conductive zones C3–C7 are more likely to result from aqueous fluids with different volumes of melts (i.e., incomplete crystallization).

5. Discussion

5.1 Migration feature of crustal materials based on the electrical resistivity model

5.1.1 Vertical migration feature

Laboratory experiments reported that when the volume fraction of melts is more than 5%, the effective viscosity can be reduced by an order of magnitude and that when the volume fraction of melts is more than 20%, the strain rate of dunites can be reduced by approximately 2 orders of magnitude (Rosenberg and Handy, 2005; Dong et al., 2020). Our results show that the volume fractions of melts in the conductive zones C1 and C2 in the middle-lower crust of the Lhasa terrane are likely more than 5%. Therefore, we surmise that the effective viscosity of these conductive zones in the middle-lower crust of the central Lhasa terrane may be reduced by an order of magnitude. This suggests the existence of large-scale rheologically weak zones. Both the middle-lower crust of the southern Lhasa terrane and the Tethys-Himalaya terrane show such a rheologically weak feature. The latest results from ambient noise tomography in the east-west direction along latitude 30°N show a low-velocity zone beneath the Xainza-Dinggye rift and adjacent regions, which could be explained by a volume fraction of 7% of melts (Li et al., 2024). This independent result is consistent and similar to the volume fraction of melts estimated for the conductive zones C1 and C2.

The electrical resistivity model shows that the conductive zones C1 and C2 are crustal scale, and an electrical resistivity model of the lithosphere (Zhang, 2017) reported conductive zones at depths of more than 80 km (lithospheric mantle) beneath the C1 and C2. Helium isotope results indicate that, taking latitude 30°N as a boundary, Helium isotopes from mantle-derived features occur in the north (central Lhasa terrane), while crust-derived features occur in the south (southern Lhasa terrane and Tethys-Himalaya terrane) (Klemperer et al., 2022). The conductive zones C1 and C2 correspond well with the locations of the mantle-derived Helium. In summary, the present study reveals that conductive zones (C1 and C2) extend to the lithospheric mantle and are compatible with the partial melting of the crust resulting from upwelling of mantle-derived materials below the Lhasa terrane (Figure 13).

The Mesozoic-Cenozoic magmatic rocks distributed in the southern Lhasa terrane are related to the partial melting of crustal materials that resulted from the upwelling of mantle-derived materials (Hou et al., 2015). However, the electrical resistivity model shows that the conductive zones C3, C4, and C5 are mainly located in the upper-middle crust, and that resistive zones, which may represent the subducted Indian Plate, are beneath these conductive zones. Therefore, this study indicates that after the large-scale magmatic activities in the southern Lhasa terrane, the northward subduction of the Indian lithospheric plate may resist the upward migration of deep materials and thermal propagation, which results in the high-resistivity feature of the lower crust and lithospheric mantle in the southern Lhasa terrane.

It is possible that there exists tear(s) in the plate, in two or more segments, which occurred along weakened zones, because of the variation of the physical characteristic and/or accumulation of strain within the subducted plate (Kennett and Furumura, 2010; Chen et al., 2015), which results in the differential subduction of the Indian lithospheric plate along strike. The subduction angle of the Indian lithospheric plate influenced the upwelling of mantle-derived materials, and tear windows related to differential subduction of different segments also contributed to the upwelling of mantle-derived materials. Meanwhile, previous studies also reported a close relationship between the tearing of the Indian lithospheric plate and the formation of the north-south rifts (Chen et al., 2015; Wang et al., 2022; Hou et al., 2023). Therefore, the difference between the central Lhasa terrane and southern

Lhasa terrane indicates that the tear windows resulted from the differential subduction of the Indian lithospheric plate beneath the Xainza-Dinggye rift mainly in the central Lhasa terrane (the northern part of the XDR). The connection of the conductive zones C1, C4, and C7 is parallel with the strike of the XDR in the subsurface, which may mean a tearing location in the Xainza-Xietongmen-Dinggye region.

5.1.2 Horizontal migration feature

The main Himalaya thrust fault (MHT) is the tectonic boundary between the present subducted Indian lithosphere and the overlying Himalaya orogenic prism and between the present subducted Indian lithosphere and the Tibetan crust, which extends from the middle crust of the Lhasa terrane in south Tibetan Plateau to the shallow area of crust in the Nepal region (e.g., Nábělek et al., 2009; Zhao et al., 2010). Seismic imaging has reported that low-velocity zones exist above the Indian lower crust along the MHT, and ductile layers related to these low-velocity zones not only are a suitable effect of the shear resulting from plate motion, but also act as migration channels of materials (Nábělek et al., 2009; Nábělek and Nábělek, 2014). The resistivity model shows that the conductive zones C3, C4, and C5 have a good connection with the conductive zones C1 and C2, which indicates that the middle-lower crustal materials in the Lhasa terrane migrated southwards along the MHT and provided the thermal source and material to maintain the partial melting in the middle-lower crust. However, both the long-distance southward migration of the crustal materials of the Lhasa terrane and the different-scale resistance of the thermal energy and material source contributed to the reduction of rheology in some areas of the migration channels, which is a possible reason why the migration channels are well depicted. The electrical resistivity model further shows that the conductive zones C3, C4, and C5 extend southward into the Tethys-Himalaya terrane at depths of 10–20 km with different degrees, and end north of the gneiss dome (Figure 5b, 5c); in contrast, the conductive zone C6 in the Tethys-Himalaya terrane extends northwards to the Lhasa terrane through the IYS (Figure 5b, 5c). The difference in extent of these two groups of conductive zones in the upper crust of the Tethys-Himalay terrane probably indicates the difference of the southern extrusion of the crustal materials from the Lhasa terrane to the Tethys-Himalaya terrane in different regions, which is controlled by tectonic-dynamic processes such as the subduction patterns of the Indian plate and metamorphism in the vicinity of the subduction channels.

The resistivity model shows that the area between the conductive zones C4 and C7 has a high-resistivity feature. Sensitivity tests demonstrate that the conductive zone C4 probably has a connection with the conductive zone C7 at depths of 20–40 km. Note that the Mabja gneiss dome corresponds well with the medium-high resistivity zones between the conductive zones C4 and C7. The geochemical data reported that multi-stage metamorphism and anatexis occurred in the Himalayan orogenic belt during the 45–15 Ma (King et al., 2011; Yu et al., 2011; Zhang et al., 2018), which formed the high-grade metamorphic rocks and leucogranite in the Tethys-Himalaya terrane (Zeng et al., 2011; Zhang et al., 2018). The Eocene-Miocene anatexis granite in the Mabja gneiss dome represents the southern extrusion of material in the Tethys-Himalaya terrane. Meanwhile, other research reported that the Himalayan leucogranite may be controlled by the high differentiation of magma that resulted from long-distance migration (Wu et al., 1998). Furthermore, other studies indicated that the southern extrusion of the Asian materials either ended at the gneiss dome or showed a discontinuous pattern, which was influenced by the gneiss dome (Nelson et al., 1996; Wu et al., 1998; Beaumont et al., 2001). Thermochronology studies yield estimates of middle-Miocene cooling ages in the Mabja dome (Lee et al., 2006), and, with the decrease of temperature, the resistivity of the upper-crust beneath the Mabja gneiss dome increased, which may be a possible reason why a moderately-resistive zone is observed beneath the Mabja gneiss dome.

As mentioned above, before the cooling event in the Mabja gneiss dome during the middle Miocene, the conductive zones C4 and C7 were connected, which represented the southern extrusion of the crustal materials from the Lhasa terrane to the Tethys-Himalaya terrane. Geochemical isotope results reported that the hydrothermal activities in the Dinggye regions since ~0.5 Ma were controlled by the partial melting of crust that resulted from the upwelling of asthenospheric materials (Hou and Li, 2004), which indicates that the thermal materials also continue to migrate southwards to the Tethys-Himalay terrane along the migration channels. The Helium isotope results in the Dinggye region demonstrated that the radioactive heat and tectonic heat, both of which were related to the Indian lithospheric plate and/or thrust structure (e.g., the STDS) (Hou and Li, 2004; Klemperer et al., 2022), can provide the thermal energy to maintain the partial melting of the conductive zone C7. Therefore, the conductive zone C7 may be controlled by the multi-period tectonic-dynamic processes.

Previous studies demonstrated that the "southeastern escape of crustal materials" is a possible horizontal motion model for the crustal materials in the Tibetan Plateau (especially in the Lhasa terrane; e.g., Royden et al., 1997; Unsworth et al., 2005). One of the important conditions of the east-west-directed migration of crustal materials is the existence of interconnected low-viscosity zones in the middle-lower crust (e.g., Wei et al., 2010; Jin et al., 2022). Both our electrical resistivity model and the estimated volume fractions of melts/fluids indicate that the conductive zones C1 and C2 in the central Lhasa terrane contain more than 5 vol% melts and are

interconnected. Meanwhile, in the southern Lhasa terrane, except for the conductive zone C3, other areas have high resistivity, and the corresponding volume fractions of melts/fluids are low. Thus the middle-lower crust of the central Lhasa terrane meets the necessary condition for east-west-directed migration of materials, while that of the southern Lhasa terrane may not. Combined with the discussion above, our study indicates that in the process of the upwelling of mantle-derived materials, both vertical and horizontal motion are present. In the background of the south-north extrusion and east-west extension, some low-viscosity (i.e., conductive) zones in the middle-lower crust of the central Lhasa terrane are interconnected in local regions (Figure 13).

5.2 Tectonic dynamics

5.2.1 Evolution of the Xainza-Dinggye rift

Combined with the regional resistivity model of the whole Lhasa terrane (Jin et al., 2022), the conductive zones C1 and C2 appear to extend to the northern boundary of the XDR, that is, the intersection location of the XDR and the GCT in the subsurface. Therefore, the northern segment of the XDR corresponds with the conductive zones of the middle-lower crust, while the middle-lower crust of the central and southern segments of the XDR shows a high-resistivity feature. Some small-scale conductive zones (e.g., C4 and C7) are distributed in the upper crust in the vicinity of the XDR. As mentioned in Section 5.1.2, the connection of the conductive zones C1, C4, and C7 represents the southern extrusion of the crustal materials of the Lhasa terrane to the upper-middle crust of the Tethys-Himalaya terrane, and the volume fractions of melts in the conductive zones C1, C4, and C7 may be more than 5%. Taken together, this means that these four conductive zones are representative of the ductile layers beneath the XDR and its adjacent areas. In the northern segment, the ductile layers (conductive zones) are located at depths of 30–70 km in the middle-lower crust, while in the central and southern segments, the ductile layers are mainly at depths of 20–40 km in the upper-middle crust, and these crustal ductile layers may result in the decoupling of the overlying brittle crust and underlying lithosphere (e.g., Sheng et al., 2021; Jin et al., 2022). In the post-collision extension period of the Indian-Eurasion plates, these crustal ductile layers can make the stress concentrate in some areas of the shallow subsurface, and under certain condition, the brittle layers in the upper crust may exceed the elastic limit because of the concentration of stress, which can result in the deformation of the upper crust and form a series of the north-south normal faults (rifts).

In summary, our study indicates that the upwelling of the mantle-derived materials that are caused by the subduction and tearing of the Indian lithospheric plate resulted in the partial melting of the lower crust, and the melts/fluids migrated upwards to the middle crust and migrated southwards to the upper-middle crust of the Tethys-Himalaya terrane, both of which can form the large-scale crustal ductile layers, and the deformation of the brittle upper crust that caused by the ductile layers is the main dynamic mechanism of the Xainza-Dinggye rift (Figure 14). Previous studies indicated that the formation age of the northern segment of the XDR (~14 Ma; Bian et al., 2020) is earlier than that of the southern segment of the XDR (~13–10 Ma; Bian et al., 2020), which corresponds well with the dynamic processes of the XDR proposed in this study. Geochemical data reported that the formation age of the rock dykes in the Mabja gneiss dome can be traced back to 12–9 Ma (King et al., 2011), which is later than the evolution age of the southern segment of the XDR. Therefore, when the crustal materials of the Lhasa terrane migrated southwards to the upper-middle crust of the Tethys-Himalaya terrane, metamorphism and anatexis occurred in some areas of the migration channels to form the high-grade metamorphic rocks and leucogranite in the Mabja gneiss dome. With cooling below the Mabja gneiss dome during the middle Miocene, the resistivity of the crust beneath the Mabja gneiss dome and adjacent areas increased (Figure 14). Furthermore, the low-angle southern Tibetan detachment system formed in ~17 Ma also contributed to the southern migration of materials in the upper-middle lower crust of the Tethys-Himalaya terrane.

In addition, the electrical resistivity model shows that the hot springs are distributed within and in the vicinity of some middle-high conductive zones at depths of 10–20 km in the upper crust, which corresponds well with the 17 km depths of the thermal sources in the Xainza-Dinggye thermal belt reported in previous studies (e.g., Chang et al., 2017). The continuous and intense activities of the Indian-Eurasian plates resulted in deep-seated magmatic sources in the lower crust, and large-scale partial-melting area in the middle crust, and some shallow magma reservoirs with different scales at different depths in the upper crust (e.g., Jin et al., 2022; Sheng et al., 2024). The above contributed to the special thermal structure beneath the Tibetan Plateau and its surroundings.

5.2.2 Seismogenic environment in the Xainza-Xietongmen-Dinggye region

At 9:05 a.m. on January 7, 2025, a M_S6.8 (magnitude of the surface wave) earthquake occurred in the Dingri district (Figure 1; blue star), with a focus depth of 10 km (derived from the China Earthquake Network). Preliminary research showed that the seismic fault of the event was the Dengmocuo fault in the south part of the XDR in the Tethys-Himalaya terrane, and was a normal fault type (e.g., Bai et al., 2025; Zhao et al., 2025). The electrical resistivity model (Figure 5b, 5c) shows that the hypocenter is spatially located in an electrical gradient belt between conductive and re-

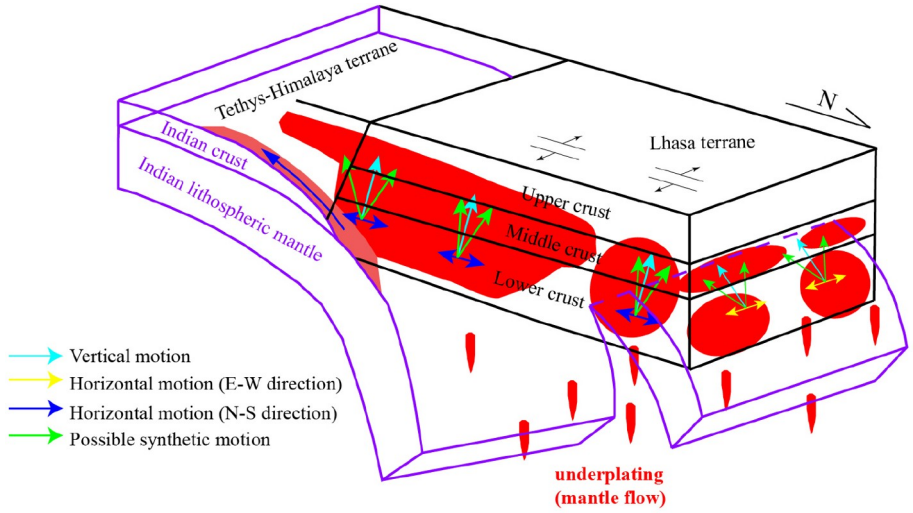

Figure 13 Proposed model for material migration.

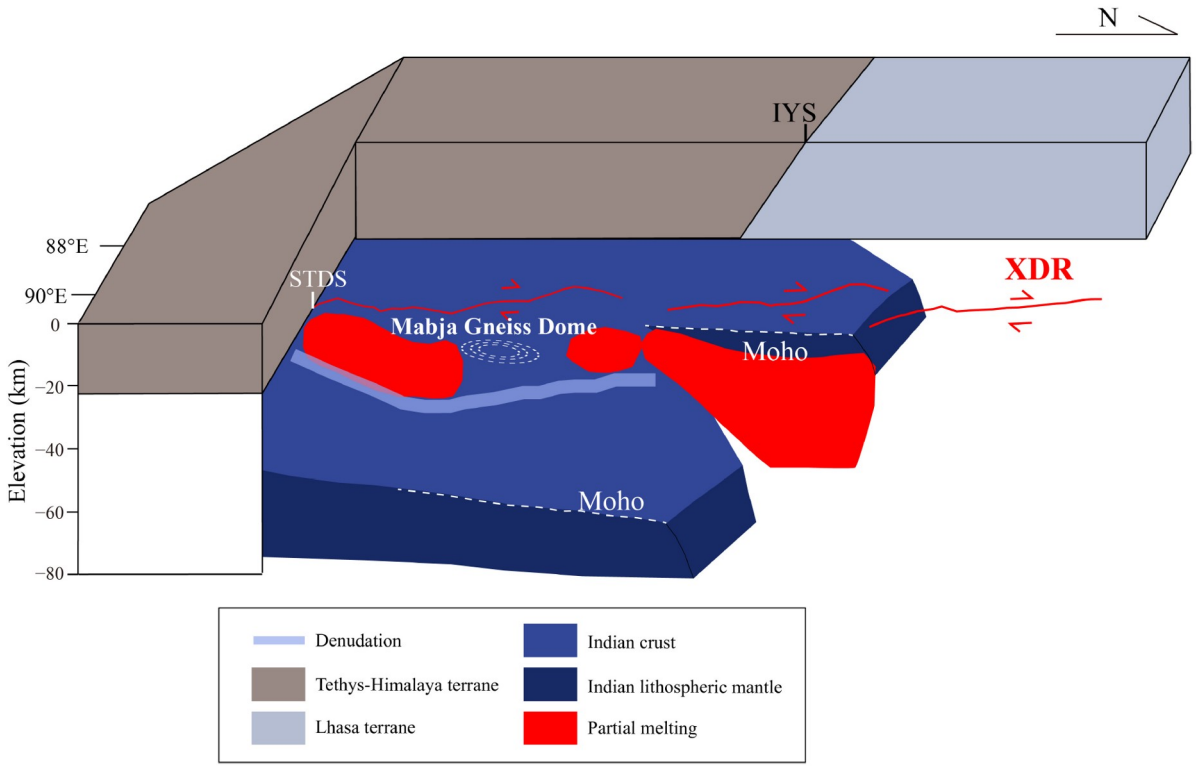

Figure 14 Sketch of the hypothesized tectonic-dynamic process in the Xainza-Xietongmen-Dinggye region.

sistive zones in the upper-middle crust of the Tethys-Himalaya terrane. Meanwhile, the hypocenters of other shallow-focus earthquakes in the Tethys-Himalaya terrane have a similar coupling feature (Figure 5b, 5c), however, the high-resistivity zones represented by the subducted Indian lithospheric plate are at depths of more than 30 km beneath these shallow-focus earthquakes. Furthermore, the shallow-focus earthquakes in the Lhasa terrane are located in the north part of the XDR, and the hypocenters are spatially located in the middle-high resitivity zones (Figure 5b, 5c), and some large-scale ductile layers (conductive zones C1 and C2) are at depths of more than 30 km beneath these shallow-focus earthquakes.

Our study suggests that the conductive zones C1 and C2 are controlled by partial melting of crust resulting from the subduction and tearing of the Indian lithospheric plate, while the conductive zones in the upper crust of the Tethys-Himalaya terrane mainly result from aqueous fluids (including

aqueous melts and saline fluids). Moreover, these are controlled by the southern extrusion of the crustal materials of the Lhasa terrane to the upper-middle crust Tethys-Himalaya terrane, and those tectonic-dynamic processes also contribute to the formation of the Xainza-Dinggye rift. Therefore, we hypothesize that the large-scale ductile layers in the middle-lower crust reduce the extension of the overlying brittle layers in depth, and that the stress is accumulated in the middle-high resistivity zones (e.g., Li L et al., 2021; Yu et al., 2022) to result in the shallow-focus earthquakes in the north, while the migration of fluids is resisted by the high resistivity block in the upper-middle crust of the Tethys-Himalaya terrane to result in stress accumulation in some regions (e.g., Zhao et al., 2012), which contributes to shallow-focus earthquakes (e.g., Dingri M_S6.8 earthquake). The results above show a close relationship between the shallow-focus earthquakes and activity of the Xainza-Dinggye rift.

The intermediate-depth earthquakes are mainly distributed in the middle-high resistivity zones that represent the subducted Indian Plate (Figure 5g, 5h). According to the Moho depth map, the hypocenters of these intermediate-depth earthquakes are mainly distributed at Moho depth and in the top part of the lithospheric mantle. Previous study reported that the intermediate-depth earthquakes are related to the subduction of the Indian plate (Liang et al., 2016). In the process of the northward subduction of the Indian plate, the Indian lithospheric mantle detached from the Indian crust and continued to subduct northwards (Klemperer et al., 2022; Jin et al., 2022; Lu et al., 2022), which may provide the necessary energy to promote the occurrence of intermediate-depth earthquakes. In the Tethys-Himalaya terrane, although the fracture zones are created by the detachment of the Indian lithospheric mantle from the Indian crust, these fracture zone may be compacted by the gravitational interaction of the overlying Indian crust, which is a possible reason why these area at depths of 60–70 km show high resistivity features.

6. Summary

In this study, an array of magnetotelluric data covering the Xainza-Xietongmen-Dinggye region is used to construct a high-resolution electrical resistivity model. Subsequently, the formation mechanism of the identified conductive zones is analyzed based on the relationship between conductivity and the volume fraction of melts/fluids. Combined with the spatiotemporal coupling relationship of the geological, geochemical, and geophysical data, we analyze the state and migration of crustal materials and their relationship with the Xainza-Dinggye rift and Mabja Gneiss Dome. In addition, we discuss the seismogenic background in this region.

Our results indicate that large-scale conductive zones in the middle-lower crust of the Lhasa terrane result from aqueous melts (partial melting) related to the upwelling of mantle-derived materials into the lower crust, which is controlled by the subduction and tearing of the Indian lithospheric plate, and the volume fractions of melts in these conductive zones are at least 5%. Accounting for the temperature at depths of 10–20 km in the upper crust, the conductive zones at different depths are more likely to be attributed to the mixture of different volume fractions of aqueous melts and saline fluids. The conductive zones in the middle-lower crust of the central Lhasa terrane gradually become wider with the shallower depths, which results from the synthetic motion of vertical and horizontal fluid migration. Furthermore, the connection of the conductive zones at different depths from the Lhasa terrane to the Tethys-Himalaya terrane represents the southern extrusion of crustal material in the Lhasa terrane to the upper crust of the Tethys-Himalaya terrane.

As mentioned above, the upwelling of the mantle-derived materials related to the tearing of the subducted Indian lithospheric plate resulted in partial melting of the middle-lower crust in the Lhasa terrane, and meanwhile, the upwelling thermal materials migrated southwards to the Tethys-Himalaya terrane. This resulted in partial melting of the upper-middle crust in the Tethys-Himalaya terrane. Following this, large-scale crustal ductile layers caused by the partial melting resulted in decoupling of the overlying crust and underlying lithosphere and the deformation of the brittle upper crust, all of which contributed to the evolution of the Xainza-Dinggre rift. In addition, the thermal materials in the upper-middle crust of the Tethys-Himalaya terrane related to the southern extrusion from the Lhasa terrane caused metamorphism and anatexis, which played an important role in the evolution of the Mabja gneiss dome. During the middle Miocene, cooling events in the Mabja gneiss dome led to an increase in the resistivity (between the conductive zones C1 and C4), and the thermal source that maintained the partial melting of the upper-middle crust in the Tethys-Himalaya terrane may have been radioactive heat and shear heat. Additionally, shallow-focus and intermediate-depth earthquakes are mainly controlled by the synergy of the tectonic dynamics, lithospheric material state, and fluid migration.

Acknowledgements *Special thanks must go to our field crews and students; this study would not have been possible without their efforts. We used the GMT software package for the production of some figures. This work was supported by the High-performance Computing Platform of China University of Geosciences, Beijing. This study was supported by the National Natural Science Foundation of China (Grant No. 42304087), the National Key R&D Program of China (Grant No. 2022YFF0800901), and the Fundamental Research Funds for the Central Universities (Grant No. 2-9-2023-202).*

Conflict of interest The authors declare that they have no conflict of interest.

References

Archie G E. 1942. The electrical resistivity log as an aid in determining some reservoir characteristics. Trans AIME, 146: 54–62

Armijo R, Tapponnier P, Mercier J L, Han T. 1986. Quaternary extension in southern Tibet: Field observations and tectonic implications. J Geophys Res, 91: 13803–13872

Bai L, Chen Z W, Wang S J. 2025. The 2025 Dingri M_S6.8 earthquake in Xizang: Analysis of tectonic background and discussion of source characteristics (in Chinese). Rev Geophys Planet Phys, 56: 258–263

Beaumont C, Jamieson R A, Nguyen M H, Lee B. 2001. Himalayan tectonics explained by extrusion of a low-viscosity crustal channel coupled to focused surface denudation. Nature, 414: 738–742

Bian S, Gong J F, Zuza A V, Yang R, Tian Y T, Ji J Q, Chen H L, Xu Q Q, Chen L, Lin X B, Cheng X G, Tu J Y, Yu X J. 2020. Late Pliocene onset of the Cona rift, eastern Himalaya, confirms eastward propagation of extension in Himalayan-Tibetan orogen. Earth Planet Sci Lett, 544: 116383

Booker J R. 2014. The magnetotelluric phasetensor: A critical review. Surv Geophys, 35: 7–40

Burg J P, Guiraud M, Chen G M, Li G C. 1984. Himalayan metamorphism and deformations in the north Himalayan Belt (southern Tibet, China). Earth Planet Sci Lett, 69: 391–400

Caldwell T G, Bibby H M, Brown C. 2004. The magnetotelluric phase tensor. Geophys J Int, 158: 457–469

Calvert A J. 2017. Continuous estimation of 3-D reflector orientations along 2-D deep seismic reflection profiles. Tectonophysics, 718: 61–71

Chang C F. 1985. Plate tectonics of the Tibetan Plateau (in Chinese). Bull Mineral Petrol Geochem, 4: 56–58

Chang M Y, Gan S S, Hu Z D, Liu Z. 2017. Geologic feature of Shenzha graben in Xizang (in Chinese). China's Manganese Ind, 35: 5–7

Chave A D, Jones A G. 2012. The Magnetotelluric Method: Theory and Practice. Cambridge: Cambridge University Press

Chen J, Gaillard F, Villaros A, Yang X, Laumonier M, Jolivet L, Unsworth M, Hashim L, Scaillet B, Richard G. 2018. Melting conditions in the modern Tibetan crust since the Miocene. Nat Commun, 9: 3515

Chen S, Zhang B, Zhang J, Wang Y, Li X, Zhang L, Yan Y, Cai F, Yue Y. 2022. Tectonic transformation from orogen-perpendicular to orogen-parallel extension in the North Himalayan Gneiss Domes: Evidence from a structural, kinematic, and geochronological investigation of the Ramba gneiss dome. J Struct Geol, 155: 104527

Chen Y, Li W, Yuan X, Badal J, Teng J. 2015. Tearing of the Indian lithospheric slab beneath southern Tibet revealed by SKS-wave splitting measurements. Earth Planet Sci Lett, 413: 13–24

Chung S L, Chu M F, Zhang Y, Xie Y, Lo C H, Lee T Y, Lan C Y, Li X, Zhang Q, Wang Y. 2005. Tibetan tectonic evolution inferred from spatial and temporal variations in post-collisional magmatism. Earth-Sci Rev, 68: 173–196

Dong H, Sun K, Egbert G, Kelbert A, Meqbel N. 2024. Hybrid CPU-GPU solution to regularized divergence-free curl-curl equations for electromagnetic inversion problems. Comput Geosci, 184: 105518

Dong H, Wei W, Jin S, Ye G, Jones A G, Zhang L T, Jing J E, Xie C L, Yin Y T. 2020. Shaping the surface deformation of central and south Tibetan Plateau: Insights from magnetotelluric array data. J Geophys Res-Solid Earth, 125: 2019JB019206

Egbert G D. 1997. Robust multiple-station magnetotelluric data processing. Geophys J Int, 130: 475–496

Egbert G D, Kelbert A. 2012. Computational recipes for electromagnetic inverse problems. Geophys J Int, 189: 251–267

Fu J G, Li G M, Wang G H, Huang Y, Zhang L K, Dong S L, Liang W. 2017. First field identification of the Cuonadong dome in southern Tibet: Implications for EW extension of the north Himalayan gneiss dome. Int J Earth Sci (Geol Rundsch), 106: 1581–1596

Glover P W J, Hole M J, Pous J. 2000. A modified Archie's law for two conducting phases. Earth Planet Sci Lett, 180: 369–383

Glover P W J. 2010. A generalized Archie's law for n phases. Geophysics, 75: E247–E265

Grujic D, Hollister L S, Parrish R R. 2002. Himalayan metamorphic sequence as an orogenic channel: Insight from Bhutan. Earth Planet Sci Lett, 198: 177–191

Hashim L, Gaillard F, Champallier R, Le Breton N, Arbaret L, Scaillet B. 2013. Experimental assessment of the relationships between electrical resistivity, crustal melting and strain localization beneath the Himalayan-Tibetan Belt. Earth Planet Sci Lett, 373: 20–30

Hashin Z, Shtrikman S. 1962. A variational approach to the theory of the effective magnetic permeability of multiphase materials. J Appl Phys, 33: 3125–3131

He Z L, Feng J Y, Zhang Y, Li P W. 2017. A tentative discussion on an evaluation system of geothermal unit ranking and classification in China (in Chinese). Earth Sci Front, 2017, 24: 168–179

Hou Z Q, Li Z Q. 2004. Possible location for underthrusting front of the Indian continent: Constraints from helium isotope of the geothermal gas in southern Tibet and eastern Tibet (in Chinese). Acta Geol Sin, 78: 482–482

Hou Z Q, Li Z Q, Qu X M, Gao Y F, Hua L C, Zheng M P, Li S R, Yuan W L. 2001. The uplift process of the Tibetan Plateau since 0.5 Ma—Evidence from hot water activities in the Gangdise Belt (in Chinese). Sci China Ser D-Earth Sci, 31: 27–33

Hou Z Q, Wang R, Zhang H J, Zheng Y C, Jin S, Thybo H, Weinberg R F, Xu B, Yang Z M, Hao A W, Gao L, Zhang L T. 2023. Formation of giant copper deposits in Tibet driven by tearing of the subducted Indian plate. Earth-Sci Rev, 243: 104482

Hou Z Q, Zheng Y C, Lu Z W, Xu B, Wang C M, Zhang H R. 2020. Growth, thickening and evolution of the thickened crust of the Tibet Plateau. Acta Geol Sin, 94: 2797–2815

Hou Z, Duan L, Lu Y, Zheng Y, Zhu D, Yang Z, Yang Z S, Wang B D, Pei Y G, Zhao Z D, McCuaig T C. 2015. Lithospheric architecture of the Lhasa terrane and itscontrol on oredeposits in the Himalayan-Tibetan orogen. Econ Geol, 110: 1541–1575

Jin S, Sheng Y, Comeau M J, Becken M, Wei W B, Ye G F, Dong H, Zhang L T. 2022. Relationship of the crustal structure, rheology, and tectonic dynamics beneath the Lhasa-Gangdese terrane (southern Tibet) based on a 3-D electrical model. J Geophys Res-Solid Earth, 127: e2022JB024318

Jones A G. 1992. Electrical conductivity of the continental lower crust. In: Fountain D M, Arculus R J, Kay R W, eds. Continental Lower Crust. Amsterdams: Elsevier B.V. 81–143

Kapp P, Guynn J H. 2004. Indian punch rifts Tibet. Geology, 32: 993–996

Kelbert A, Meqbel N, Egbert G D, Tandon K. 2014. ModEM: A modular system for inversion of electromagnetic geophysical data. Comput Geosci, 66: 40–53

Kennett B L N, Furumura T. 2010. Tears or thinning? Subduction structures in the Pacific plate beneath the Japanese Islands. Phys Earth Planet Inter, 180: 52–58

King J, Harris N, Argles T, Parrish R, Zhang H F. 2011. Contribution of crustal anatexis to the tectonic evolution of Indian crust beneath southern Tibet. Geol Soc Am Bull, 123: 218–239

Klemperer S L, Zhao P, Whyte C J, Darrah T H, Crossey L J, Karlstrom K E, Liu T Z, Winn C, Hilton D R, Ding L. 2022. Limited underthrusting of India below Tibet: ^{3}He/^{4}He analysis of thermal springs locates the mantle suture in continental collision. Proc Natl Acad Sci USA, 119: e2113877119

Langille J, Lee J, Hacker B, Seward G. 2010. Middle crustal ductile deformation patterns in southern Tibet: Insights from vorticity studies in Mabja Dome. J Struct Geol, 32: 70–85

Le Pape F, Jones A G, Unsworth M J, Vozar J, Wei W, Jin S, Ye G F, Jing J E, Dong H, Zhang L T, Xie C L. 2015. Constraints on the evolution of crustal flow beneath Northern Tibet. Geochem Geophys Geosyst, 16: 4237–4260

Lee J, Whitehouse M J. 2007. Onset of mid-crustal extensional flow in southern Tibet: Evidence from U/Pb zircon ages. Geology, 35: 45

Lee J, Hacker B R, Dinklage W S, Wang Y, Gans P, Calvert A, Wan J L, Chen W J, Blythe A E, McClelland W. 2000. Evolution of the Kangmar

Dome, southern Tibet: Structural, petrologic, and thermochronologic constraints. Tectonics, 19: 872–895
Lee J, McClelland W, Wang Y, Blythe A, McWilliams M. 2006. Oligocene-Miocene middle crustal flow in southern Tibet: Geochronology of Mabja Dome. Geol Soc London Spec Publ, 268: 445–469
Li D D, Tian X B, Liang X F, Nie S T. 2024. Different formation modes of the north-south-trending rifts in southern Tibet: Implications from ambient noise tomography. Geophys Res Lett, 51: e2024GL108254
Li L, Zhang X, Liao J, Liang Y, Dong S. 2021. Geophysical constraints on the nature of lithosphere in central and eastern Tibetan Plateau. Tectonophysics, 804: 228722
Li S, Unsworth M J, Booker J R, Wei W, Tan H, Jones A G. 2003. Partial melt or aqueous fluid in the mid-crust of Southern Tibet? Constraints from INDEPTH magnetotelluric data. Geophys J Int, 153: 289–304
Li Y H, Gao T M, Wu Q J. 2014. Crustal thickness map of the Chinese mainland from teleseismic receiver functions. Tectonophysics, 611: 51–60
Liang H D, Jin S, Wei W B, Gao R, Ye G F, Zhang L T, Yin Y T, Lu Z W. 2018. Lithospheric electrical structure of the middle Lhasa terrane in the south Tibetan Plateau. Tectonophysics, 731-732: 95–103
Liang X F, Chen Y, Tian X B, Chen Y J, Ni J, Gallegos A, Klemperer S L, Wang M L, Xu T, Sun C Q, Si S K, Lan H Q, Teng J W. 2016. 3D imaging of subducting and fragmenting Indian continental lithosphere beneath southern and central Tibet using body-wave finite-frequency tomography. Earth Planet Sci Lett, 443: 162–175
Liang X, Zhou S, Chen Y J, Jin G, Xiao L, Liu P, Fu Y, Tang Y, Lou X, Ning J. 2008. Earthquake distribution in southern Tibet and its tectonic implications. J Geophys Res, 113: 2007JB005101
Lu Z W, Guo X Y, Gao R, Murphy M A, Huang X F, Xu X, Li S Z, Li W H, Zhao J M, Li C S, Xiang B. 2022. Active construction of southern most Tibet revealed by deep seismic imaging. Nat Commun, 13: 3143
Luo M, Wood J R, Cathles L M. 1994. Prediction of thermal conductivity in reservoir rocks using fabric theory. J Appl Geophys, 32: 321–334
Mechie J, Sobolev S V, Ratschbacher L, Babeyko A Y, Bock G, Jones A G, Nelson K D, Solon K D, Brown L D, Zhao W. 2004. Precise temperature estimation in the Tibetan crust from seismic detection of the α-β quartz transition. Geology, 32: 601–604
Molnar P, Tapponnier P. 1978. Active tectonics of Tibet. J Geophys Res, 83: 5361–5375
Nábělek J, Hetényi G, Vergne J, Sapkota S, Kafle B, Jiang M, Su H, Chen J, Huang B S, Team H C. 2009. Underplating in the Himalaya-Tibet collision zone revealed by the Hi-CLIMB experiment. Science, 325: 1371–1374
Nábělek P I, Nábělek J L. 2014. Thermal characteristics of the Main Himalaya Thrust and the Indian lower crust with implications for crustal rheology and partial melting in the Himalaya orogen. Earth Planet Sci Lett, 395: 116–123
Nelson K D, Zhao W, Brown L D, Kuo J, Che J, Liu X, Klemperer S L, Makovsky Y, Meissner R, Mechie J, Kind R, Wenzel F, Ni J, Nabelek J, Leshou C, Tan H, Wei W, Jones A G, Booker J, Unsworth M, Kidd W S F, Hauck M, Alsdorf D, Ross A, Cogan M, Wu C, Sandvol E, Edwards M. 1996. Partially molten middle crust beneath southern Tibet: Synthesis of Project INDEPTH results. Science, 274: 1684–1688
Ni H W, Zhang L, Guo X. 2016. Water and partial melting of Earth's mantle. Sci China Earth Sci, 59: 720–730
Parkinson W D. 1959. Directions of rapid geomagnetic fluctuations. Geophys J Int, 2: 1–14
Ramberg H. 1980. Diapirism and gravity collapse in the Scandinavian Caledonides. J Geol Soc, 137: 261–270
Rippe D, Unsworth M J. 2010. Quantifying crustal flow in Tibet with magnetotelluric data. Phys Earth Planet Inter, 179: 107–121
Roberts J J, Tyburczy J A. 1999. Partial-melt electrical conductivity: Influence of melt composition. J Geophys Res, 104: 7055–7065
Rosenberg C L, Handy M R. 2005. Experimental deformation of partially melted granite revisited: Implications for the continental crust. J Metamorph Geol, 23: 19–28
Royden L H, Burchfiel B C, King R W, Wang E, Chen Z, Shen F, Liu Y. 1997. Surface deformation and lower crustal flow in eastern Tibet. Science, 276: 788–790
Sheng Y, Jin S, Comeau M J, Dong H, Zhang L T, Lei L L, Li B C, Wei W B, Ye G F, Lu Z W. 2021. Lithospheric structure near the northern Xainza-Dinggye Rift, Tibetan Plateau—Implications for rheology and tectonic dynamics. J Geophys Res-Solid Earth, 126: e2020JB021442
Sheng Y, Jin S, Comeau M J, Hou Z Q, Becken M, Dong H, Zhang L, Wei W B, Ye G F. 2023a. Evidence for partial melting and alkali-rich fluids in the crust from a 3-D electrical resistivity model in the vicinity of the Coqen region, western Lhasa terrane, Tibetan Plateau. Earth Planet Sci Lett, 619: 118316
Sheng Y, Jin S, Comeau M J, Hou Z Q, Zhang L T, Wei W B, Ye G F. 2023b. Relationship between the migration of crustal material, normal faulting, and gneiss domes in the vicinity of the Dinggye region, central part of the Tethys-Himalaya terrane: Insights from the 3-D electrical structure. Tectonophysics, 869: 230100
Sheng Y, Jin S, Comeau M J, Hou Z Q, Yin Y T, Zhang L T, Wei W B, Ye G F. 2024. Crustal conductivity footprint of the Miocene porphyry copper polymetallic deposits in the Gangdese metallogenic belt, Tibetan Plateau. Ore Geol Rev, 168: 106033
Somerton W H. 1992. Thermal properties and temperature-related behavior of rock/fluid systems. Developments in Petroleum Science, Volume 37. Elsevier
Sun Y J, Dong S W, Fan T Y, Zhang H, Shi Y L. 2013. 3D rheological structure of the continental lithosphere beneath China and adjacent regions. Chin J Geophys, 56: 546–558
Tapponnier P, Peltzer G, Le Dain A Y, Armijo R, Cobbold P. 1982. Propagating extrusion tectonics in Asia: New insights from simple experiments with plasticine. Geology, 10: 611
Tapponnier P, Xu Z, Roger F, Meyer B, Arnaud N, Wittlinger G, Yang J. 2001. Oblique stepwise rise and growth of the Tibet Plateau. Science, 294: 1671–1677
Teyssier C, Whitney D L. 2002. Gneiss domes and orogeny. Geology, 30: 1139
Unsworth M J, Jones A G, Wei W, Marquis G, Gokarn S G, Spratt J E. 2005. Crustal rheology of the Himalaya and Southern Tibet inferred from magnetotelluric data. Nature, 438: 78–81
Wang H, Elliott J R, Craig T J, Wright T J, Liu-Zeng J, Hooper A. 2015. Normal faulting sequence in the Pumqu-Xainza rift constrained by InSAR and teleseismic body-wave seismology. Geochem Geophys Geosyst, 15: 2947–2963
Wang R, Weinberg R F, Zhu D C, Hou Z Q, Yang Z M. 2022. The impact of a tear in the subducted Indian plate on the Miocene geology of the Himalayan-Tibetan orogen. GSA Bull, 134: 681–690
Wei W B, Unsworth M, Jones A, Booker J, Tan H, Nelson D, Chen L S, Li S S, Solon K, Bedrosian P, Jin S, Deng M, Ledo J, Kay D, Roberts B. 2001. Detection of widespread fluids in the Tibetan crust by magnetotelluric studies. Science, 292: 716–719
Wei W B, Jin S, Ye G F, Deng M, Jing J E, Unsworth M, Jones A G. 2010. Conductivity structure and rheological property of lithosphere in Southern Tibet inferred from super-broadband magnetotelluric sounding. Sci China Earth Sci, 53: 189–202
Weidelt P. 1985. Construction of conductance bounds from magnetotelluric impedances. J Geophys, 57: 191–206
Whitney D L, Teyssier C, Vanderhaeghe O. 2004. Gneiss domes and crustal flow. In: Whitney D L, Teyssier C, Siddoway C S, eds. Gneiss Domes in Orogeny. Geological Society of America Special Paper, 380. Boulder, Colorado. 15–33
Wu C D, Nelson K D, Wortman G, Samson S D, Yue Y J, Li J X, Kidd W S F, Edwards M A. 1998. Yadong cross structure and South Tibetan Detachment in the east central Himalaya (89°–90°E). Tectonics, 17: 28–45
Wu F Y, Liu Z C, Liu X C, Ji W Q. 2015. Himalayan leucogranites (in Chinese). Acta Petrol Sin, 31: 1–36
Xiong S Q, Yang H, Ding Y Y, Li Z K. 2016. Characteristics of Chinese continent Curie point isotherm (in Chinese). Chin J Geophys, 59: 3604–

3617
Xu Z Q, Yang J S, Li H B, Zhang J X, Zeng L S, Jiang M. 2006. The Qinghai-Tibet Plateau and continental dynamics: A review on terrain tectonics, collisional orogenesis, and process and mechanisms for the rise of the plateau (in Chinese). Geol China, 33: 221–238
Xu Z Q, Yang J S, Hou Z Q, Zhang Z M, Zeng L S, Li H B, Zhang J X, Li Z H, Ma X X. 2016. The progress in the study of continental dynamics of the Tibetan Plateau (in Chinese). Geol China, 43: 1–42
Xue S, Chen Y, Liang H, Li X, Liang X, Ma X, Lu Z, Bai D, Yan Y. 2021. Deep electrical resistivity structure across the Gyaring Co Fault in Central Tibet revealed by magnetotelluric data and its implication. Tectonophysics, 809: 228835
Yang X Z. 2014. Electrical petrology: Principles, methods and advances (in Chinese). Sci Sin Terr, 44: 1884–1900
Yardley B W D, Valley J W. 1997. The petrologic case for a dry lower crust. J Geophys Res, 102: 12173–12185
Yin A. 2004. Gneiss domes and gneiss dome systems. Special Paper of the Geological Society of America, 380
Yin A, Harrison T M. 2000. Geologic evolution of the Himalayan-Tibetan orogen. Annu Rev Earth Planet Sci, 28: 211–280
Yu J J, Zeng L S, Liu J, Gao L E, Xie K J. 2011. Early Miocene leucogranites in Dinggye area, southern Tibet: Formation mechanism and tectonic implications (in Chinese). Acta Petrol Sin, 27: 1961–1972
Yu L, Evans R L, Edwards R N. 1997. Transient electromagnetic responses in seafloor with triaxial anisotropy. Geophys J Int, 129: 292–304
Yu N, Wang X, Li D, Li X, Wang E, Kong W, Li T. 2022. The mechanism of deep material transport and seismogenic environment of the Xiaojiang fault system revealed by 3-D magnetotelluric study. Sci China Earth Sci, 65: 1128–1145
Zeng L S, Gao L E, Xie K J, Liu-Zeng J. 2011. Mid-Eocene high Sr/Y granites in the northern Himalayan gneiss domes: Melting thickened lower continental crust. Earth Planet Sci Lett, 303: 251–266
Zhang J J. 2002. Structural characteristics of middle and southern Xainza-Dinggye Normal Fault System and its relationship to Southern Tibetan Detachment System. Chin Sci Bull, 47: 1063
Zhang J J. 2007. A review on the extensional structures in the northern Himalaya and southern Tibetan (in Chinese). Geol Bull China, 26: 639–649
Zhang J J, Guo L. 2007. Structure and geochronology of the southern Xainza-Dinggye rift and its relationship to the South Tibetan detachment system. J Asian Earth Sci, 29: 722–736
Zhang J J, Santosh M, Wang X X, Guo L, Yang X Y, Zhang B. 2012. Tectonics of the northern Himalaya since the India-Asia collision. Gondwana Res, 21: 939–960
Zhang L T. 2017. A review of recent developments in the study of regional lithospheric electrical structure of the Asian continent. Surv Geophys, 38: 1043–1096
Zhang L T, Jin S, Wei W B, Ye G F, Jing J E, Dong H, Xie C L. 2015. Lithospheric electrical structure of South China imaged by magnetotelluric data and its tectonic implications. J Asian Earth Sci, 98: 178–187
Zhang Z M, Kang D Y, Ding H X, Tian Z L, Dong X, Qin S K, Mu H C, Li M M. 2018. Partial melting of Himalayan orogen and formation mechanism of leucogranite (in Chinese). Earth Sci, 43: 82–98
Zhao G Z, Unsworth M J, Zhan Y, Wang L F, Chen S B, Jones A G, Tang J, Xiao Q B, Wang J K, Cai J T, Li T, Wang Y Z, Zhang J H. 2012. Crustal structure and rheology of the Longmenshan and Wenchuan M_w 7.9 earthquake epicentral area from magnetotelluric data. Geology, 40: 1139–1142
Zhao J M, Yuan X H, Liu H B, Kumar P, Pei S P, Kind R, Zhang Z J, Teng J W, Ding L, Gao X, Xu Q, Wang W. 2010. The boundary between the Indian and Asian tectonic plates below Tibet. Proc Natl Acad Sci USA, 107: 11229–11233
Zhao W H, Xu Q, Ji F, Xie M L, Fan X M, Wang Y S, Zhao J J. 2025. Deformation field characteristics and site effect analysis of the M_S 6.8 Dingri earthquake in Xizang on January 7, 2025 (in Chinese). J Chengdu Univ Technol (Sci Technol Ed), 52: 173–184
Zheng Y, Chen Y, Chen R, Dai L. 2022. Tectonic evolution of convergent plate margins and its geological effects. Sci China Earth Sci, 65: 1247–1276
Zhu D C, Zhao Z D, Niu Y, Mo X X, Chung S L, Hou Z Q, Wang L Q, Wu F Y. 2011. The Lhasa terrane: Record of a microcontinent and its histories of drift and growth. Earth Planet Sci Lett, 301: 241–255
Zhu D C, Zhao Z D, Niu Y, Dilek Y, Wang Q, Ji W H, Dong G C, Sui Q L, Liu Y S, Yuan H L, Mo X X. 2012. Cambrian bimodal volcanism in the Lhasa terrane, southern Tibet: Record of an early Paleozoic Andean-type magmatic arc in the Australian Proto-Tethyan margin. Chem Geol, 328: 290–308
Zhu D C, Zhao Z D, Niu Y, Dilek Y, Hou Z Q, Mo X X. 2013. The origin and pre-Cenozoic evolution of the Tibetan plateau. Gondwana Res, 23: 1429–1454
Zou J, Wu B, Ma S X, Chen N, Xie W, Zou H M, Yang D B. 2023. Geothermal genesis and resource potential of Kaga in Xietongmen County in Tibet (in Chinese). Hydrogeol Eng Geol, 50: 207–216

(Editorial handling: Shuang LIU)